Defense Threat Reduction Agency
8725 John J. Kingman Road, MS 6201
Fort Belvoir, VA 22060-6201

DTRA-TR-03-1

TECHNICAL REPORT

Synthesizing High-Frequency (1-25 HZ) Regional Phases at Large Distances (>1000 KM) Using Generalized Screen Propagators (GSP)

Approved for public release; distribution is unlimited.

September 2004

DSWA 01-97-1-0004

Ru-Shan Wu
Xiao-Bi Xie
Xianyun Wu

Prepared by:
University of California
Institute of Geophysics and
Planetary Physics
1156 High Street
Santa Cruz, CA

DESTRUCTION NOTICE

FOR CLASSIFIED documents, follow the procedures in DoD 5550.22-M, National Industrial Security Program Operating Manual, Chapter 5, Section 7 (NISPOM) or DoD 5200.1-R, Information Security Program Regulation, Chapter 1X.

FOR UNCLASSIFIED limited documents, destroyed by any method that will prevent disclosure of contents or reconstruction of the document.

Retention of this document by DoD contractors is authorized in accordance with DoD 5220.22-M, Industrial Security Manual.

PLEASE NOTIFY THE DEFENSE THREAT REDUCTION AGENCY, ATTN: BDLMI, 8725 JOHN J. KINGMAN ROAD, MS-6201, FT BELVOIR, VA 22060-6201, IF YOUR ADDRESS IS INCORRECT, IF YOU WISH IT DELETED FROM THE DISTRIBUTION LIST, OR IF THE ADDRESSEE IS NO LONGER EMPLOYED BY YOUR ORGANIZATION.

DISTRIBUTION LIST UPDATE

This mailer is provided to enable DTRA to maintain current distribution lists for reports. (We would appreciate you providing the requested information.)

- ☐ Add the individual listed to your distribution list.
- ☐ Delete the cited organization/individual.
- ☐ Change of address.

Note:
Please return the mailing label from the document so that any additions, changes, corrections or deletions can be made easily. For distribution cancellation or more information call DTRA/BDLMI (703) 767-4725.

NAME: _____

ORGANIZATION: _____

OLD ADDRESS	NEW ADDRESS
_____	_____
_____	_____
_____	_____

TELEPHONE NUMBER: ( ) _____

DTRA PUBLICATION NUMBER/TITLE	CHANGES/DELETIONS/ADDITONS, etc. *(Attach Sheet if more Space is Required)*
_____	_____
_____	_____
_____	_____

DTRA or other GOVERNMENT CONTRACT NUMBER: _____

CERTIFICATION of NEED-TO-KNOW BY GOVERNMENT SPONSOR (if other than DTRA):

SPONSORING ORGANIZATION: _____

CONTRACTING OFFICER or REPRESENTATIVE: _____

SIGNATURE: _____

REPORT DOCUMENTATION PAGE

Form Approved
OMB No. 0704-0188

1. REPORT DATE *(DD-MM-YYYY)*	2. REPORT TYPE	3. DATES COVERED *(From - To)*
00-09-2005	Technical	970501 - 000430

4. TITLE AND SUBTITLE

Synthesizing High-Freguency (1-25 HZ) Regional Phases at Large Distances (1 > 1000 KM) Using Generalized Screen Propagators (GSP)

5a. CONTRACT NUMBER
C-DTRA 01-97-1-0004

5b. GRANT NUMBER

5c. PROGRAM ELEMENT NUMBER
PE- 4662

6. AUTHOR(S)

Ru-Shan Wu, Xiao-Bi Xie, and Xianyun Wu

5d. PROJECT NUMBER
PR - AB

5e. TASK NUMBER
TA - KB

5f. WORK UNIT NUMBER
WU - DH64117

7. PERFORMING ORGANIZATION NAME(S) AND ADDRESS(ES)

University of California
Institute of Geophysics and Planetary Physics
1156 High Street
Santa Cruz, CA 95062

8. PERFORMING ORGANIZATION REPORT NUMBER

9. SPONSORING/MONITORING AGENCY NAME(S) AND ADDRESS(ES)

Defense Threat Reduction Agency
8725 John J. Kingman Road, MS 6201
Fort Belvoir, VA 22060-6201

TDND/D. Barber

10. SPONSOR/MONITOR'S ACRONYM(S)

11. SPONSOR/MONITOR'S REPORT NUMBER(S)
DTRA-TR-00-32

12. DISTRIBUTION/AVAILABILITY STATEMENT
Approved for public release; distribution is unlimited.

13. SUPPLEMENTARY NOTES
This work was sponsored by the Defense Threat Reduction Agency under RDT&E RMC code B 4662 D AB KB 64117 5P00 A 25904D

14. ABSTRACT

Based on the half-space screen propagator developed in our previous project, we successfully extended the method to the case of irregular surface topography by the conformal and non-conformal topographic transforms. Its validity and potential applications have been numerically demonstrated by comparing with the boundary element method. The new method can handle combined effects of small-scale heterogeneities (random media) and rough random topography on Lg wave propagation. It is also 2-3 orders of magnitude faster than the finite difference method. In the P-SV wave case, reflected plane waves from a free surface are incorporated into the elastic screen method for Lg wave simulation. Due to the presence of a surface wave (Rayleigh wave), both the real and imaginary parts of the wavenumber must be included. Body waves including reflected and converted waves are calculated using real wavenumber integration; surface wave are calculated with imaginary wavenumber integration. The comparison between results from numerical test and the wavenumber integration method shows excellent agreement. Numerical results show that this is a promising method for simulating path effects in different regions for various monitoring discriminants such as Pn/Lg or Sn/Lg, etc.

15. SUBJECT TERMS

Seismic wave propagation
Lg-wave
CTBT
Generalized screen method

16. SECURITY CLASSIFICATION OF:			17. LIMITATION OF ABSTRACT	18. NUMBER OF PAGES	19a. NAME OF RESPONSIBLE PERSON
a. REPORT	b. ABSTRACT	c. THIS PAGE			19b. TELEPHONE NUMBER *(Include area code)*
Unclassified	Unclassified	Unclassified	SAR	54	

CONVERSION TABLE

Conversion Factors for U.S. Customary to metric (SI) units of measurement.

MULTIPLY → BY → TO GET

TO GET ← BY ← DIVIDE

angstrom	1.000 000 x E -10	meters (m)
atmosphere (normal)	1.013 25 x E +2	kilo pascal (kPa)
bar	1.000 000 x E +2	kilo pascal (kPa)
barn	1.000 000 x E -28	meter^2 (m^2)
British thermal unit (thermochemical)	1.054 350 x E +3	joule (J)
calorie (thermochemical)	4.184 000	joule (J)
cal (thermochemical/cm^2)	4.184 000 x E -2	mega joule/m^2 (MJ/m^2)
curie	3.700 000 x E +1	*giga bacquerel (GBq)
degree (angle)	1.745 329 x E -2	radian (rad)
degree Fahrenheit	$t_k = (t°f + 459.67)/1.8$	degree kelvin (K)
electron volt	1.602 19 x E -19	joule (J)
erg	1.000 000 x E -7	joule (J)
erg/second	1.000 000 x E -7	watt (W)
foot	3.048 000 x E -1	meter (m)
foot-pound-force	1.355 818	joule (J)
gallon (U.S. liquid)	3.785 412 x E -3	meter^3 (m^3)
inch	2.540 000 x E -2	meter (m)
jerk	1.000 000 x E +9	joule (J)
joule/kilogram (J/kg) radiation dose absorbed	1.000 000	Gray (Gy)
kilotons	4.183	terajoules
kip (1000 lbf)	4.448 222 x E +3	newton (N)
kip/inch^2 (ksi)	6.894 757 x E +3	kilo pascal (kPa)
ktap	1.000 000 x E +2	newton-second/m^2 (N-s/m^2)
micron	1.000 000 x E -6	meter (m)
mil	2.540 000 x E -5	meter (m)
mile (international)	1.609 344 x E +3	meter (m)
ounce	2.834 952 x E -2	kilogram (kg)
pound-force (lbs avoirdupois)	4.448 222	newton (N)
pound-force inch	1.129 848 x E -1	newton-meter (N-m)
pound-force/inch	1.751 268 x E +2	newton/meter (N/m)
pound-force/foot^2	4.788 026 x E -2	kilo pascal (kPa)
pound-force/inch^2 (psi)	6.894 757	kilo pascal (kPa)
pound-mass (lbm avoirdupois)	4.535 924 x E -1	kilogram (kg)
pound-mass-foot^2 (moment of inertia)	4.214 011 x E -2	kilogram-meter^2 (kg-m^2)
pound-mass/foot^3	1.601 846 x E +1	kilogram-meter^3 (kg/m^3)
rad (radiation dose absorbed)	1.000 000 x E -2	**Gray (Gy)
roentgen	2.579 760 x E -4	coulomb/kilogram (C/kg)
shake	1.000 000 x E -8	second (s)
slug	1.459 390 x E +1	kilogram (kg)
torr (mm Hg, 0^0 C)	1.333 22 x E -1	kilo pascal (kPa)

*The bacquerel (Bq) is the SI unit of radioactivity; 1 Bq = 1 event/s.

**The Gray (GY) is the SI unit of absorbed radiation.

TABLE OF CONTENTS

TABLE OF FIGURES

SUMMARY

Based on the half-space screen propagator developed in our previous project, we successfully extended the method to the case of irregular surface topography by the conformal and non-conformal topographic transforms. Its validity and potential applications have been numerically demonstrated by comparisonsonson with the boundary element method. The new method can handle combined effects of small-scale heterogeneities (random media) and rough random topography on Lg wave propagation. It is also 2-3 orders of magnitude faster than the finite difference method. In the P-SV wave case, reflected plane waves from a free surface are incorporated into the elastic screen method for Lg wave simulation. Due to the presence of a surface wave (Rayleigh wave), both the real and imaginary parts of the wave-number must be included. Body waves including reflected and converted waves are calculated using real wavenumber integration; surface waves are calculate with imaginary wavenumber integration. The comparison between results from numerical tests and the wavenumber integration method shows excellent agreement. Numerical results show that this is a promising method for simulating path effects in different regions for various monitoring discriminants such as Pn/Lg or Sn/Lg, etc.

1. INTRODUCTION

Modeling high-frequency regional wave propagation in complex crustal waveguides is one of the most challenging problems in theoretical and computational seismology. A good understanding of the propagation, scattering, attenuation and wave-type conversion of regional phases is essential for the application of regional waves in monitoring a CTBT (Comprehensive Nuclear-Test-Ban Treaty). Complex waveguide structures, including rough topography, uneven Moho discontinuities and volume heterogeneities of all scales, will affect the propagation of the Lg wave. High-frequency regional waves up to 20 Hz have been observed over distances ranging from a few hundred *km* to more than one thousand *km* (e.g., Ni et al., 1996; Herrmann et al., 1997; Lay et al., 1999). For these high-frequency waves, new mechanisms may be involved in their propagation, scattering and attenuation. The availability of numerical tools that can simulate and analyze Lg wave propagation under these environments is crucial. Discrimination and yield estimation at regional distances for very low-yield events are even more demanding of these tools. To simulate regional phases, traditional techniques usually use overly simplified crust models or do calculations for very limited frequencies and distances. The current DoD/DSWA project is targeted to develop a very flexible, while still efficient, numerical method for simulating high-frequency, long-distance Lg wave propagation in a realistic crustal waveguide environment.

[2] Recently, the generalized screen method has been introduced into seismic wave simulations and applied to problems of both exploration seismology and earthquake seismology. The generalized screen propagator (GSP) is based on the one-way wave equation and the one-return approximation. The propagator neglects backscattered waves but correctly handles all forward propagated energy, e.g., multiple forward scattering, focusing/defocusing, diffraction, interference and conversion between different wave types. Significant progress has been made in the development of an elastic complex screen (ECS) method for modeling elastic wave propagation in complicated structures (Wu, 1994, 1996; Xie and Wu, 1995; Wild and Hudson, 1998; Wu and Wu, 1998, 1999). The method is two to three orders of magnitude faster than the elastic finite-difference method for medium size 3D problems. The screen method has been

successfully used for forward modeling (Wu, 1994; Wu and Huang, 1995; Xie and Wu 1995, 1996, 1999, 2000; Wu and Wu,1999) and as backpropagators for seismic imaging/migration in both acoustic and elastic media (Wu and Xie 1994; Huang and Wu 1996; Huang et al., 1999a,b; Jin and Wu, 1999; Jin et al., 1999, Xie and Wu, 1998).

In the crustal waveguide environment, Lg is a guided wave composed of upgoing and downgoing waves bouncing between the free surface and other major geological discontinuities such as the Moho and Conrad. Beyond the critical angle, they are consistently dominated by small angle waves trapped in the crustal waveguide. Major wave energy is carried by forward propagating waves. Therefore the neglect of backscattered waves in the propagation will not change the main features of regional waves in most cases. By neglecting backscattering in the theory, the method becomes a forward marching algorithm, the next step of propagation only depends on the present values of the wavefield in a transverse cross-section and the heterogeneities between the two cross-sections. The savings of computing time and storage memory are enormous. This makes it a viable method for high-frequency, long-distance Lg wave propagation in 3D elastic problems.

A half-space generalized screen propagator has been introduced (Wu et al., 1996, 2000a) to accommodate the free-surface boundary condition and to handle SH wave propagation in complex crustal waveguides. The new propagator has been calibrated extensively against several full-wave numerical methods for different crustal models. In these, the wavenumber integration method is chosen for flat structures and the finite-difference method is used for laterally heterogeneous crustal waveguides. Excellent agreement is obtained and shows the validity and accuracy of the new one-way method. For a crust model with a propagation distance of 250 km and a dominant frequency of 0.5 Hz, the GSP method is about 300 times faster than the finite-difference method with similar accuracy. The method also been used to simulate Lg propagation as well as related energy partitioning and attenuation in random media (Wu et al., 2000b). It is found that the leakage attenuation caused by large-angle forward scattering may play an important role for Lg attenuation and blockage in some regions. The equivalent Q of leakage attenuation versus normalized scale length (ka) of random heterogeneities agrees well with observations and scattering theory.

In the current DoD/DSWA project, the half-space GSP method for SH waves has been

extended to include irregular topography using both conformal and non-conformal coordinate transforms. In the conformal transform method, the coordinate system is rotated according to the local topographic slope, and the mirror image method is applied to the local plane surface. The non-conformal method is a surface flattening transform that transforms the surface perturbation into modified volume perturbations. The former method is suitable for dealing with smoothly varying topography, while the latter can treat rough but moderate topography. To show their validity and potential applications, numerical examples are conducted and compared with the results from the boundary element method. A preliminary investigation of the combined effects of small-scale heterogeneities (random media) and rough random surface on Lg wave propagation is carried out.

Another new development under this project is a 2D P-SV elastic complex screen propagator for crustal waveguides with a flat free surface. Plane wave reflection coefficients are introduced to calculate down-going waves. Due to the existance of a surface (Rayleigh) wave, both the real and imaginary parts of the wavenumber must be included. Body waves, including the reflected and converted waves, can be calculated using real wavenumber integration, while surface waves can be calculated with imaginary wavenumber integration. The comparison between the results of the numerical tests and the wavenumber integration method shows excellent agreement. The seismic responses for a more realistic crustal model, the Flora-Asnes model, are simulated using the elastic screen method.

2. SH-WAVE CASE

A half-space GSP method for modeling Lg wave propagation in smoothly varying, heterogeneous crustal waveguides has been developed by Wu et al. (2000a). The detailed derivation of the method and numerical tests as well as its application can be found in the papers of Wu et al. (2000a,b). In this section, we focus on extending the half-space GSP method to handle an irregular free surface through application of conformal and non-conformal coordinate transforms. For a complete description of the extended GSP method, the half-space screen propagator is briefly summerized.

2.1 A BRIEF SUMMARY OF THE HALF-SPACE SCREEN PROPAGATOR

For a 2D SH problem, only the y-component of the displacement field, denoted as u, exists. With the perturbation method, the medium and the wave field are decomposed into

$$\rho = \rho_0 + \delta\rho;\ \mu = \mu_0 + \delta\mu;\ u = u^0 + U$$

where ρ_0 and μ_0 are the density and shear rigidity of the background medium, $\delta\rho$ and $\delta\mu$ are the corresponding perturbations, u^0 is the primary field and U is the scattered field. The SH wave equation in the frequency domain can be written as

$$\mu_0\nabla^2 u + \omega^2\rho_0 u = -[\omega^2\delta\rho u + \nabla\cdot\delta\mu\nabla u] \tag{1}$$

For each step of the marching algorithm under the forward-scattering approximation, the total field at x_1 is calculated as the sum of the primary field propagating in the half-space from x' to x_1, and the scattered field caused by the heterogeneities in the thin-slab between x' and x_1. The thickness of the slab should be made thin enough to ensure the validity of the local Born

approximation. The Green's function in the homogeneous half-space can be obtained by the image method. The stress should vanish at the free surface $z = 0$. We consider only the one-way wave propagation in the positive x-direction. The scattered field by the thin-slab can be calculated by (Wu et al., 2000a)

$$\begin{aligned} U(x_1, K_z) &= U_\rho(x_1, K_z) + U_\mu(x_1, K_z) \\ U_\rho(x_1, K_z) &= ik \int_{x'}^{x_1} dx e^{i\gamma(x_1 - x)} \mathcal{C}[\frac{k}{\gamma} \varepsilon_\rho(z) u_0(z)] \\ U_\mu(x_1, K_z) &= ik \int_{x'}^{x_1} dx e^{i\gamma(x_1 - x)} \Big\{ \mathcal{C}[\varepsilon_\mu(z) \bar{\partial}_x u_0(z)] \\ &- i\mathcal{S}[\frac{K_z}{\gamma} \varepsilon_\mu(z) \bar{\partial}_z u_0(z)] \Big\} \end{aligned} \tag{2}$$

where

$$\varepsilon_\rho(\mathbf{r}) = \frac{\delta\rho(\mathbf{r})}{\rho_0}, \quad \varepsilon_\mu(\mathbf{r}) = \frac{\delta\mu(\mathbf{r})}{\mu_0},$$

and $\gamma = \sqrt{k^2 - K_z^2}$ is the propagating wave number in the x-direction and K_z is transverse wavenumber along the z-axis, and

$$\bar{\partial}_x = \frac{1}{ik} \frac{\partial}{\partial x}, \quad \bar{\partial}_z = \frac{1}{ik} \frac{\partial}{\partial z}$$

In the above equations, $\mathcal{C}[f(z)]$ and $\mathcal{S}[f(z)]$ are the cosine and sine transforms. u_0, $\bar{\partial}_x u_0$ and $\bar{\partial}_z u_0$ can be calculated by

$$u_0(x, z) = \mathcal{C}^{-1}[e^{i\gamma'(x - x')} u_0(x', K_z')] \tag{3}$$

$$\begin{aligned} \bar{\partial}_x u_0(x, z) &= \mathcal{C}^{-1}[e^{i\gamma'(x - x')} \frac{\gamma'}{k} u_0(x', K_z')] \\ \bar{\partial}_z u_0(x, z) &= i\mathcal{S}^{-1}[e^{i\gamma'(x - x')} \frac{K_z'}{k} u_0(x', K_z')] \end{aligned} \tag{4}$$

where $\mathcal{C}^{-1}[F(K_z)]$ and $\mathcal{S}^{-1}[F(K_z)]$ are the inverse transforms of $\mathcal{C}[f(z)]$ and $\mathcal{S}[f(z)]$. The above equations are the general wide-angle formulation. When the energy of crustal guided waves are mainly carried by small-angle waves (with respect to the horizontal direction), the *phase-screen* approximation can be invoked to simplify the theory and calculations. Summing up the primary and scattered fields and invoking the Rytov transform result in the dual-domain (phase space), the expression of the phase-screen propagator for this case is

$$u(x_1, K_z) \approx e^{i\gamma(x_1 - x')} \mathcal{C}\left[e^{ikS_s(z)} u_0(x', z)\right] \tag{5}$$

where $e^{ikS_s(z)}$ is the phase delay operator with

$$S_s(z) = \frac{1}{2}\int_{x'}^{x_1} dx[\varepsilon_\rho(x,z) - \varepsilon_\mu(x,z)] \approx \Delta x \bar{\varepsilon}_s(z). \tag{6}$$

Here $\bar{\varepsilon}_s(z)$ is the average S-wave slowness perturbation over the thin slab at depth z,

$$\bar{\varepsilon}_s(z) = \frac{1}{x_1 - x'}\int_{x'}^{x_1} dx \frac{s(x,z) - s_0}{s_0}$$

with $s(x,z) = 1/v(x,z)$, and $\Delta x = (x_1 - x')$ is the thin-slab thickness. Equation (5) is the SH phase-screen propagator for the half-space. It has a similar form as the whole space propagator with the Fourier transform replaced by a cosine transform.

2.2 CONFORMAL COORDINATE TRANSFORM FOR IRREGULAR TOPOGRAPHY

Equation (5) is the SH phase-screen propagator for the half-space with a flat surface. In the case of irregular topography, the global mirror symmetry for the problem no longer exists. However, if a first order approximation (local plane-surface approximation) for the topography is taken, we can modify the mirror image method to a local mirror image method and apply the corresponding coordinate transform to obtain a GSP solution for this case.

Figure 1 shows the geometry of the derivation. Assume u_0^+ is the incident field on S^+, then u_0^- on S^- is also known as the mirror image of u_0^+ about the local plane surface. The total wavefield composed of S^+ and S^- is the sum of the primary field which propagates in the homogeneous background medium and the scattered field which is generated by the local heterogeneities in the thin-slab. The effects of the heterogeneities and the topography can be calculated separately for each step of the GSP method. The effect of the slant free-surface can be incorporated into the propagation integral. Assume $u_t(x,z)$ is the total field including the scattering effect of the volume heterogeneities. The field $u(x_1,z_1)$ in front of the integral surface can be calculated by the Kirchhoff integral

$$\begin{aligned} u(x_1,z_1) &= \int_S ds \left\{ g(x,z;x_1,z_1)\frac{\partial u_t(x,z)}{\partial n} - \frac{\partial g(x,z;x_1,z_1)}{\partial n} u_t(x,z) \right\} \\ &= \int_{S^-} ds\,\{\cdots\} + \int_{S^+} ds\,\{\cdots\} \end{aligned} \tag{7}$$

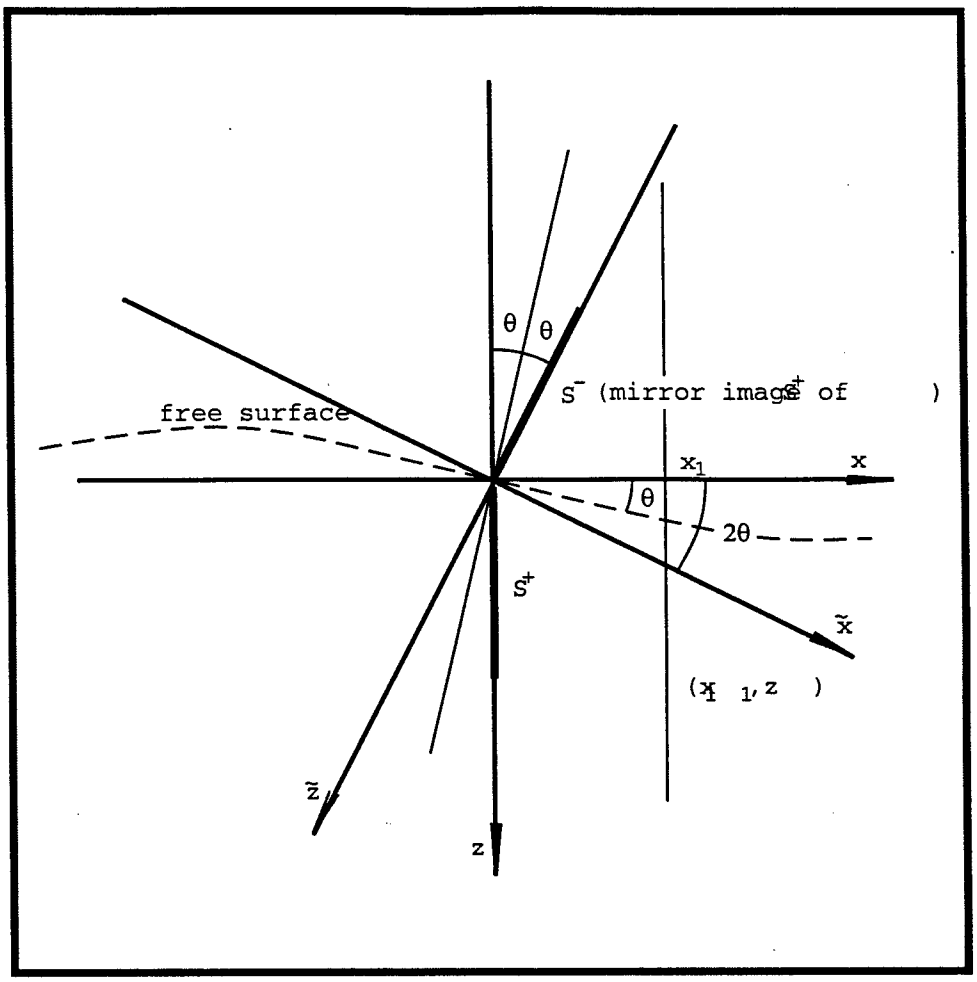

Figure 1. Geometry of the coordinate transform.

where $g(.)$ is the Green's function for the full space with homogeneous velocity distribution, S is the integration surface and S^+ and S^- are the lower and upper half surfaces, respectively. The Rayleigh integral can be used to replace the Kirchhoff integral for each half surface integral. For the lower half-space the contribution of S^+ is

$$\begin{aligned} u_t^+(x_1,z_1) &= -2\int_0^\infty dz u_t^+(x,z)\frac{\partial g(x,z;x_1,z_1)}{\partial n} \\ &= \frac{1}{2\pi}\int dK_T e^{iK_T z_1} u_t^+(x_1,K_T) \end{aligned} \tag{8}$$

where

$$u_t^+(x_1,K_T) = e^{i\gamma(x_1-x)}\int_0^\infty dz_1 u_t^+(x,z)e^{-iK_T z_1} \tag{9}$$

Here $u_t^+(x,z)$ is the total field equal to the sum of incident field $u_0^+(x,z)$ and the scattered field $U^+(x,z)$ caused by the heterogeneities within the slab between x and x_1 (Wu, 1994; Wu et al., 2000a). If we put the slab entrance at $x = x'$ and the field on the screen S^+ at the entrance as $u_t^+(x',z')$, then

$$u_t^+(x',z') = u_0^+(x',z') + U^+(x',z') \tag{10}$$

$$\begin{aligned} U^+(x',z') &= k^2\int_{x'}^{x_1} dx e^{-i\gamma(x_1-x')}\int_0^\infty dz \{g(x_1,z_1;x,z)\varepsilon_\rho(x,z)u_0(x,z) \\ &- \frac{1}{k^2}\nabla g(x_1,z_1;x,z)\cdot\varepsilon_\mu(x,z)\nabla u_0(x,z)\Big\} \end{aligned} \tag{11}$$

For the bent upper half screen, we perform a coordinate transform by clockwise rotation of 2θ to a new coordinate system $(\tilde{x},\tilde{z})$. The relation connecting the two systems is

$$\tilde{x} = x\cos 2\theta + z\sin 2\theta \tag{12}$$

$$\tilde{z} = -x\sin 2\theta + z\cos 2\theta \tag{13}$$

In the new system, the surface S^- is parallel to the $\tilde{z}$-axis, so that

$$u_t^-(\tilde{x}_1,\tilde{K}_T) = e^{i\tilde{\gamma}(\tilde{x}_1-\tilde{x}')}\int_{-\infty}^0 d\tilde{z}' u_t^-(\tilde{x}',\tilde{z}')e^{-i\tilde{K}_T\tilde{z}'} \tag{14}$$

where $u_t^-(\tilde{x}',-\tilde{z}') = u_t^+(x',z')$. The field in the space domain can be obtained by synthesizing the contributions from all the plane waves

$$u_t^-(\tilde{x}_1,\tilde{z}) = \int d\tilde{K}_T e^{i\tilde{\gamma}(\tilde{x}_1-\tilde{x}')}e^{i\tilde{K}_T\tilde{z}}u_t^-(\tilde{x}',\tilde{K}_T) \tag{15}$$

where

$$u_t^-(\tilde{x}',\tilde{K}_T) = \int_{-\infty}^0 d\tilde{z}' u_t^-(\tilde{x}',\tilde{z}')e^{-i\tilde{K}_T\tilde{z}'}. \tag{16}$$

Transforming back to the original coordinate system,

$$u_t^-(x_1,z_1) = \int d\tilde{K_T} \exp\left\{ i\left[(\tilde{\gamma}\cos 2\theta - \tilde{K_T}\sin 2\theta)(x_1 - x') + (\tilde{\gamma}\sin 2\theta + \tilde{K_T}\cos 2\theta) z_1 \right] \right\} u_t^-(\tilde{x'}, \tilde{K_T}) \tag{17}$$

If we transform the $(\tilde{k_T}, \tilde{\gamma})$ system into (K_T, γ),

$$u_t^-(x_1,z_1) = \int dK_T u_t^-(\tilde{x'}, K_T\cos 2\theta - \gamma \sin 2\theta) e^{i\gamma(x_1 - x')} e^{iK_T z_1} \tag{18}$$

The total field is a summation of the contributions from both $u^+(x_1,z_1)$ and $u_t^-(x_1,z_1)$

$$u(x_1,z_1) = \int dK_T e^{i\gamma(x_1-x')} e^{iK_T z_1} \left[u_t^+(x', K_T) + u_t^-(\tilde{x'}, K_T\cos 2\theta - \gamma\sin 2\theta) \right] \tag{19}$$

The wavenumber integral can also be done by a FFT.

When small-angle waves prevail such as in the case of Lg propagation, the spectral interpolation in equation (19), which is tricky and even unstable in some cases, can be avoided and replaced by operations in the space domain using a narrow-angle wave approximation. From (19), it can be seen that to calculate the reflection response we need to find the spectral components $u_t^+(-\tilde{K_T})$. We will try to obtain the approximate space-domain operations corresponding to the wavenumber-domain interpolation. We know

$$u_t^+(-\tilde{K_T}) = \int_0^\infty dz e^{i(-K_T\cos 2\theta + \gamma \sin 2\theta)z} u_t^+(z) \tag{20}$$

With the narrow-angle approximation, $\gamma \approx k$, therefore,

$$u_t^+(-\tilde{K_T}) = \int_0^\infty dz' e^{iK_T z'} \left[\frac{1}{\cos 2\theta} e^{ik(\tan 2\theta)z'} u_t^+(z'/\cos 2\theta) \right] \tag{21}$$

We see that the corresponding operations for wavenumber-domain interpolation in the space-domain are a modulation plus a coordinate stretching.

2.3 NON-CONFORMAL COORDINATE TRANSFORM FOR IRREGULAR TOPOGRAPHY

An alternative to using the GSP method for solving a range-dependent boundary condition problem is to employ a simple flattening transformation given by Beillis & Tappert (1979). The

transformation is defined as

$$\begin{cases} \chi = x \\ \zeta = z - h(x) \end{cases} \tag{22}$$

where $h(x)$ is the height function of free surface. Equation (22) shows that the transformation gives only a shift to depth variable z, i.e., depth measurement starts from the free surface. Under the above transformation, the medium parameters in the new coordinate $\{\chi, \zeta\}$ can be expressed by $\hat{\mu}(\chi, \zeta) = \hat{\mu}(x, z - h(x)) = \mu(x, z)$ and $\hat{\rho}(\chi, \zeta) = \hat{\rho}(x, z - h(x)) = \rho(x, z)$.

Strictly speaking, there is no one-to-one relationship to the displacement fields of the two different coordinate systems $\{x, z\}$ and $\{\chi, \zeta\}$. However, if $h(x)$ is smooth enough and the height fluctuations are small, the displacement field $u(x, z)$ may be approximated by $\hat{u}(\chi, \zeta)$, i.e.,

$$u(x, z) \approx \hat{u}(\chi, \zeta) = \hat{u}(x, z - h(x)) \tag{23}$$

Substituting eqs (22) and (23) into the SH wave equation results in

$$\begin{aligned} &\frac{\partial}{\partial \chi}\hat{\mu}(\chi, \zeta)\frac{\partial \hat{u}(\chi, \zeta)}{\partial \chi} + \frac{\partial}{\partial \zeta}\hat{\mu}(\chi, \zeta)\frac{\partial \hat{u}(\chi, \zeta)}{\partial \zeta} = -\hat{\rho}(\chi, \zeta)\omega^2 \hat{u}(\chi, \zeta) \\ &\quad + \hat{\mu}(\chi, \zeta)\left\{2h'(x)\frac{\partial^2 \hat{u}(\chi, \zeta)}{\partial \chi \partial \zeta} + h''(x)\frac{\partial \hat{u}(\chi, \zeta)}{\partial \zeta} - (h'(x))^2\frac{\partial^2 \hat{u}(\chi, \zeta)}{\partial \zeta^2}\right\}. \end{aligned} \tag{24}$$

The simple surface flattening transformation introduces three extra terms proportional to the slope of the free surface. At first glance, it seems that the transformation makes the problem more complicated. But it turns a complex waveguide with an irregular surface into a simple one with a flat surface. Under the new coordinate system $\{\chi, \zeta\}$, the boundary condition becomes

$$\hat{\mu}\frac{\partial \hat{u}}{\partial \zeta}(\chi, \zeta = 0) = 0 \tag{25}$$

Using $\hat{\rho}(\chi, \zeta) = \rho_0 + \delta\hat{\rho}(\chi, \zeta)$ and $\hat{\mu}(\chi, \zeta) = \mu_0 + \delta\hat{\mu}(\chi, \zeta)$ Equation (24) can be rewritten as

$$\left(\hat{\nabla}^2 + k_0^2\right)\hat{u}(\chi, \zeta) = -k_0^2\left\{\hat{F}_V(\chi, \zeta) + \hat{F}_S(\chi, \zeta)\right\}\hat{u}(\chi, \zeta) \tag{26}$$

where $k_0 = \omega/v_0$, $v_0 = \sqrt{\mu_0/\rho_0}$ and the operators are

$$\hat{F}_V(\chi, \zeta) = \hat{\varepsilon}_\rho(\chi, \zeta) + \frac{1}{k_0^2}\hat{\nabla} \cdot \hat{\varepsilon}_\mu \hat{\nabla} \tag{27}$$

$$\hat{F}_S(\chi, \zeta) = -\frac{1}{k_0^2}\frac{\hat{\mu}}{\mu_0}\left[h''(x)\frac{\partial}{\partial \zeta} + 2h'(x)\frac{\partial^2}{\partial \chi \partial \zeta} - (h'(x))^2\frac{\partial^2}{\partial \zeta^2}\right]. \tag{28}$$

Equation (26) describes SH wave propagation in a homogeneous medium (background medium), but with non-zero equivalent volume forces. The equivalent volume forces $\hat{F}_V(\chi,\zeta)$ and $\hat{F}_S(\chi,\zeta)$ are from the volume heterogeneities and the surface flattening transformation, respectively. We assume that the change of the fields caused by such volume forces is small when compared with the primary background field. Thus perturbation theory can be applied to solve equation (26). Using Green's theorem, the scattered field by the equivalent forces can be written as

$$U(\chi_1,k_\zeta) = k_0^2 \int_V d^2V g^h(\chi_1,k_\eta;\chi,\zeta)\left[\hat{F}_V(\chi,\zeta)+\hat{F}_S(\chi,\zeta)\right]\hat{u}(\chi,\zeta) \tag{29}$$

where the 2D volume integration is over the volume V including all the heterogeneities in the modeling space. g^h is a half-space scalar Green's function (Wu et al., 2000a).

Comparing equations (26) and (1), we see that the only difference between the two equations is the additional term $\hat{F}_S(\chi,\zeta)$. Therefore we can apply the half-space GSP (generalized screen propagator) developed by Wu et al. (2000a) to the calculation of equation (26). Under the forward-scattering approximation, for each step of the marching algorithm, the total field at χ_1 is calculated as the sum of the primary field which is the field free-propagated in the half-space from χ' to χ_1, and the scattered field caused by the heterogeneities in the thin-slab between χ' and χ_1. The thickness of the slab should be made thin enough to ensure the validity of the local Born approximation. Under this condition, the Green's function can be approximated by the homogeneous half-space Green's function. Using the image method, Wu et al. (2000a) derived a half-space Green's function as

$$g_0^h(\chi_1,k_\zeta;\chi,\zeta) = \frac{i}{2\gamma}e^{i\gamma(\chi_1-\chi)}2cos(k_\zeta\zeta) \tag{30}$$

The scattered field at the exit χ_1 of the thin slab by the volume heterogeneities $\hat{F}_V$ is

$$\begin{aligned} U_{\hat{F}_V}(\chi_1,k_\zeta) &= \frac{ik_0^2}{2\gamma}\int_{\chi'}^{\chi_1} dx e^{i\gamma(\chi_1-\chi)}\left\{\mathcal{C}\left[\frac{k_0}{\gamma}\hat{\varepsilon}_\rho(\zeta)\hat{u}_0(\zeta)-\hat{\varepsilon}_\mu(\zeta)\bar{\partial}_\chi\hat{u}_0(\zeta)\right]\right. \\ &\left. +i\mathcal{S}\left[\frac{k_\zeta}{\gamma}\hat{\varepsilon}_\mu(\zeta)\bar{\partial}_\zeta\hat{u}_0(\zeta)\right]\right\} \end{aligned} \tag{31}$$

where $\hat{u}_0(\zeta)$ is the incident field at the entrance χ' of the thin slab. In a similar way, we can obtain the scattered field at the exit χ_1 by the equivalent force $\hat{F}_S$

$$U_{\hat{F}_S}(\chi_1,k_\zeta) = \frac{i}{2\gamma}\int_{\chi'}^{\chi_1} d\chi e^{i\gamma(\chi_1-\chi)}\mathcal{C}\left\{\frac{\hat{\mu}(\zeta)}{\mu_0}\left[-2h'(x)A+(h'(x))^2B-h''(x)D\right]\right\} \tag{32}$$

where

$$A = \frac{\partial^2 u_0(\chi,\zeta)}{\partial\zeta\partial\chi} = -i\mathcal{S}^{-1}\left[k'_\zeta\gamma' e^{i\gamma'(x-x')}\hat{u}_0(\chi',k'_\zeta)\right] \quad (33)$$

$$B = \frac{\partial^2 u_0(\chi,\zeta)}{\partial\zeta^2} = -\mathcal{C}^{-1}\left[k'^2_\zeta e^{i\gamma'(x-x')}\hat{u}_0(\chi',k'_\zeta)\right] \quad (34)$$

$$D = \frac{\partial u_0(\chi,\zeta)}{\partial\zeta} = -\mathcal{S}^{-1}\left[k'_\zeta e^{i\gamma'(x-x')}\hat{u}_0(\chi',k'_\zeta)\right] \quad (35)$$

Equations (31-35) are the dual-domain expressions of the wide-angle thin-slab propagator for SH problems in an arbitrary half-space model with arbitrary heterogeneities and an irregular surface.

Small-angle approximation

When the energy of crustal guided waves is carried mainly by small-angle waves (with respect to the horizontal direction), the small-angle approximations can be invoked to simplify the theory and calculations. For small-angle waves, $k_\zeta \ll \gamma \approx \gamma' \approx k_0$, $U_{\hat{F}_V}(\chi,k_\zeta)$ can be approximated by

$$U_{\hat{F}_V}(\chi,k_\zeta) \approx ik_0 e^{i\gamma\Delta\chi}\mathcal{C}\left[\mathcal{S}_s(\zeta)\hat{u}_0(\chi',\zeta)\right] \quad (36)$$

where $\Delta\chi = \chi_1 - \chi'$ is thickness of the thin slab, and

$$\mathcal{S}_s(\zeta) = \frac{1}{2}\int_{\chi'}^{\chi_1} d\chi\left[\hat{\varepsilon}_\rho(\chi,\zeta) - \hat{\varepsilon}_\mu(\chi,\zeta)\right] \quad (37)$$

For $U_{\hat{F}_S}(\chi,k_\zeta)$, substituting equations (33- 35) into (32), we have

$$\begin{aligned} U_{\hat{F}_S}(\chi_1,k_\zeta) = {} & \frac{i}{2\gamma}\int_{\chi'}^{\chi_1} d\chi e^{i\gamma(\chi_1-\chi)}\int_0^\infty d\zeta 2cos(k_\zeta\zeta)\frac{\hat{\mu}(\zeta)}{\mu_0}\int_{-\infty}^{\infty} dk'_\zeta e^{i\gamma'(x-x')}e^{ik'_\zeta\zeta} \\ & \left[2h'(x)k'_\zeta\gamma' - ih''(x)k'_\zeta - h'(x)^2k'^2_\zeta\right]\hat{u}_0(\chi',k'_\zeta) \end{aligned} \quad (38)$$

For a sufficiently smooth $h(x)$ with respect to x, under the small-angle approximation, the last two terms in the above equation are high-order small quantities. Neglecting the last two terms, we obtain

$$\begin{aligned} U_{\hat{F}_S}(\chi_1,k_\zeta) &= \frac{i}{2}e^{i\gamma\Delta\chi}\int_0^\infty d\zeta 2cos(k_\zeta\zeta)\frac{\hat{\mu}(\zeta)}{\mu_0}\int_{\chi'}^{\chi_1} d\chi 2h'(x)\int_{-\infty}^{\infty} dk'_\zeta e^{ik'_\zeta\zeta}k'_\zeta\hat{u}_0(\chi',k'_\zeta) \\ &= -\mathcal{Z}(\chi_1)e^{i\gamma\Delta\chi}\mathcal{C}\left\{\frac{\hat{\mu}(\zeta)}{\mu_0}\mathcal{S}^{-1}\left[k'_\zeta\hat{u}_0(\chi',k'_\zeta)\right]\right\} \end{aligned} \quad (39)$$

with

$$\mathcal{Z}(\chi_1) = h(x_1) - h(x') \quad (40)$$

It is clear that under the small-angle approximation the scattered field $U_{\hat{F}_S}$ is propotional to the height difference of the adjacent two screens for each forward step. For an upward slope, $\mathcal{Z}(\chi) < 0$, the scattered field is in-phase with the background field and strengthens the background field, while for a downward slope, $\mathcal{Z}(\chi) > 0$, the scattered field is out-phase with the background field and weakens the background field. The total field can be obtained through summing the primary field which freely propagates in the background medium and the scattered fields (36) and (39)

$$\begin{aligned}\hat{u}(\chi_1, k_\zeta) &= e^{i\gamma\Delta\chi}\mathcal{C}\left\{\hat{u}_0(\chi',\zeta) + ik_0\mathcal{S}_s(\zeta)\hat{u}_0(\chi',\zeta) - \mathcal{Z}(\chi_1)\frac{\hat{\mu}(\zeta)}{\mu_0}\mathcal{S}^{-1}\left[k'_\zeta\hat{u}_0(\chi',k'_\zeta)\right]\right\} \\ &\approx e^{i\gamma\Delta\chi}\mathcal{C}\left\{e^{ik_0\mathcal{S}_s(\zeta)}\mathcal{C}^{-1}\left[\hat{u}_0(\chi',k'_\zeta)\right] - \mathcal{Z}(\chi_1)\frac{\hat{\mu}(\zeta)}{\mu_0}\mathcal{S}^{-1}\left[k'_\zeta\hat{u}_0(\chi',k'_\zeta)\right]\right\}. \qquad (41)\end{aligned}$$

Equation (41) is the dual-domain expression of the small-angle approximation for SH wave simulation in complex waveguides with arbitrary heterogeneities and irregular surfaces.

2.4 NUMERICAL VERIFICATIONS AND SIMULATION EXAMPLES

The validity and accuracy of the GSP method applied to uniform crustal waveguides have been tested by comparing to the finite difference and reflectivity methods (Wu, et. al., 2000a,b). In this section we show some examples demonstrating the validity and the potential of the GSP with coordinate transforms applied to crustal waveguides with topography compared to the boundary element method.

Figure 2 shows the synthetic seismograms for a Gaussian hill model using the conformal screen method. The Gaussian hill is represented by $h(x) = -h_0 e^{-\frac{(x-x_0)^2}{2\sigma^2}}$ with $x_0 = 62.25km$, $h_0 = 4km$, $\sigma = 9.129km$. Synthetic seismograms calculated with the more accurate boundary element method (Fu and Wu, 1999) are also given as a reference . The solid lines represent the screen method and the dashed lines represent the boundary element method. The comparison indicates that the screen method gives a satisfactory result. It correctly modeled waveforms between 60 and 70 km distance, where two reflections from the convex free surface interfere with each other and generate complex waveforms. Note that the coordinate stretch $z/cos2\theta$ increases very fast with large angle θ, the conformal screen method works only for smoothly varying topography.

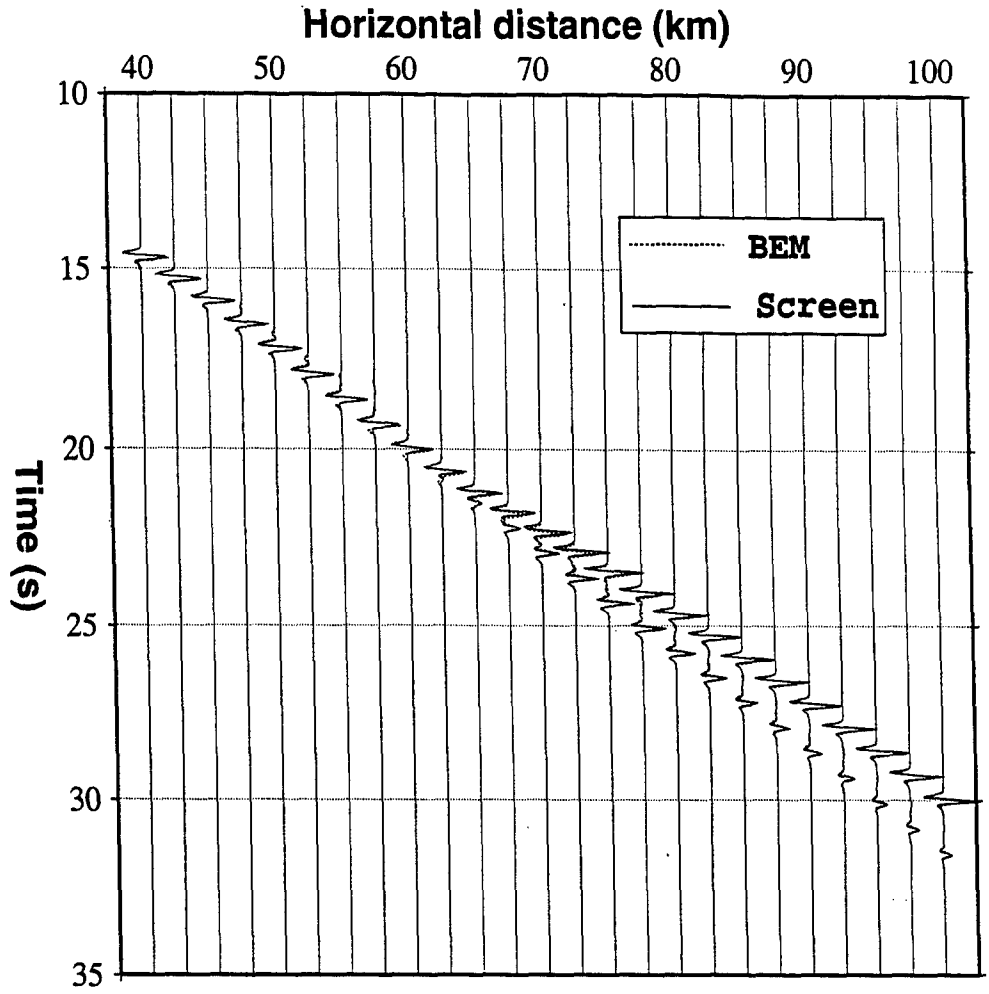

Figure 2. Synthetic seismograms using the conformal transform method (solid lines). For the calculation, dx=dz=0.25km and dt=0.05sec., the source is located at a horizontal location of 0 km, a depth of 32km and the dominant frequency of source time function is 3Hz. Receivers are on the free surface. The dashed lines are calculated with boundary element (BE) method and used as a reference (They overlie the solid lines very closely). For the calculation of the BE method, each wavelength contains 5 boundary elements at least (Fu and Wu, 1999).

Figure 3 shows the synthetic seismograms using the non-conformal screen method for the Gaussian hill model used in Figure 2. The excellent agreement between the screen method and boundary element method is clear except in the vicinity of the hill top where a small discrepancy exists both in wave shapes and amplitudes. The error will decrease when the step length Δx reduces. For forward marching algorithms, the step length Δx may be adjusted according to the roughness of topography. The more severe the topography, the finer the Δx should be. The non-conformal screen method can handle more severe topography than the conformal screen method.

Figure 5 shows a comparison of synthetic seismograms and attenuation between the screen method and the boundary element method applied to a crustal waveguide with a rough random surface shown in Figure 4. For the rough random surface, the correlation length is 2.5km, RMS height fluctuation is 0.6km (range -1.5 to 1.75 km), the mean height is -0.11 km. Figure 5 shows a comparison of synthetic seismograms calculated by the non-conformal screen method and the BE method, and the corresponding energy attenuation curves, respectively. The source is located at a depth of 8 km, the dominant frequency of the source time function is 1Hz. The thick smoothly varying curve in Figure 5b is the energy distribution for a flat free surface. We see that except for large-angle Moho reflections, the results of the screen method agree well with those of the BE method. However, for this example, the screen method took about 35 minutes, but the BE method took about 72 hours.

With the extension of the screen propagator for handling surface topography, Lg wave propagation in more realistic crustal waveguides with both volume heterogeneities and surface topography can be simulated. Figures 6-8 show an investigation of the combined effects of rough topography and volume heterogeneity on Lg wave propagation using the extended screen method. The rough topography is the same as shown in Figure 4. The heterogeneities are only for velocity variation. The heterogentity correlation lengths are 6 km in range and 4 km in depth, RMS are 5% and 10%, respectively. The source is located at a depth of 8 km. The dominant frequencies of the source time function are 0.5Hz in Figure 6, 1Hz in Figure 7 and 2Hz in Figure 8, respectively. The corresponding dominant wavelengths are 7 km, 3.5 km and 1.75 km, respectively. The thickly dashed line calculated by the finite-difference method for an uniform crustal waveguide, is used as a reference. We see from Figures 6-8 that random heterogeneities combined with rough topography drastically increase the attenuation of high frequency Lg waves.

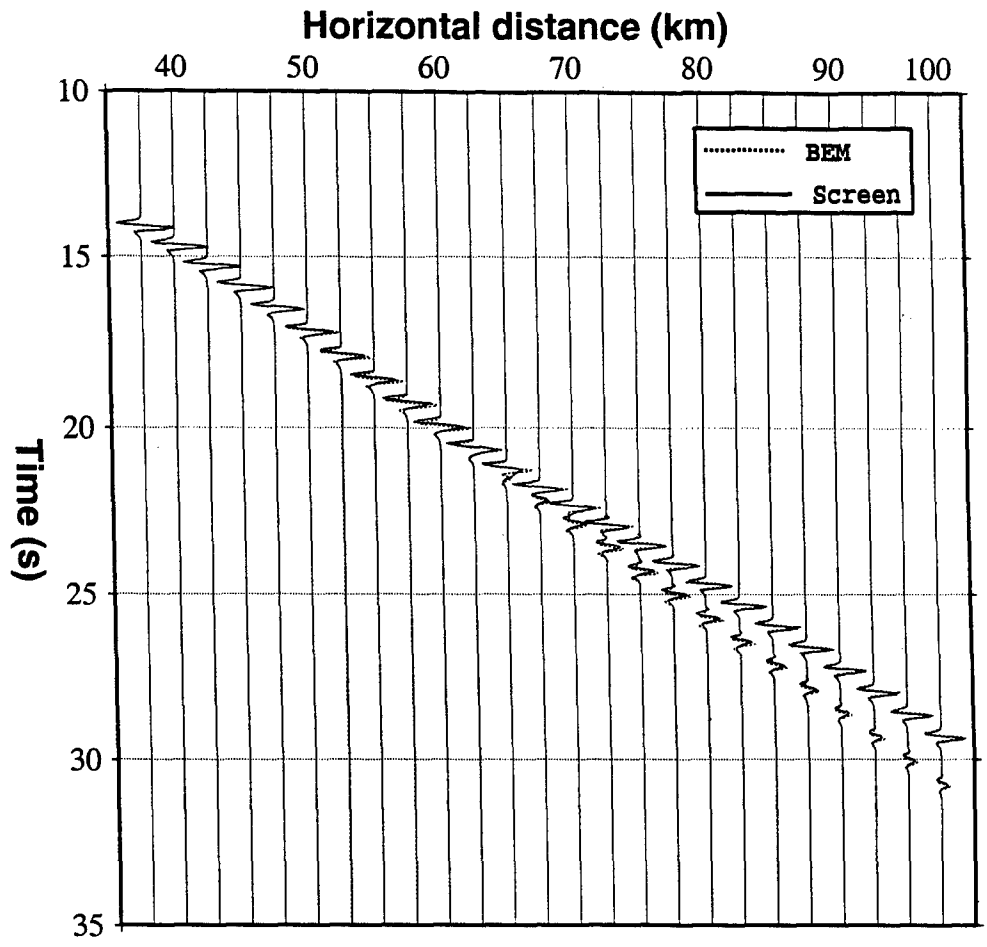

Figure 3. Synthetic seismograms using the non-conformal transform method (solid lines). For the calculation, dx=0.125km, dz=0.25km and dt=0.05sec. Source is located at the depth of 32km and the dominant frequency of source time function is 3Hz. Receivers are on free surface. The dashed lines are calculated with the boundary element (BE) method and used as a reference. For the calculation of the BE method, each wavelength contains 5 boundary elements at least (Fu and Wu, 1999).

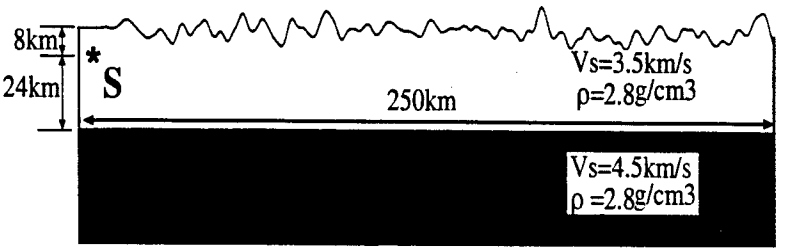

Figure 4. A crustal model with rough random surface. The correlation length is 2.5km, RMS height fluctuation is 0.6 km (range -1.5 to 1.75 km), the mean height is -0.11 km.

Attenuation and variation of Lg waves with distance are related to frequency, the characteristic length of random heterogeneities, and roughness of the surface. This example shows that the screen method can handle the effects of both volume heterogeneities and moderately rough topography on Lg wave propagation at long propagation distances and high frequencies.

2.5 BOUNDARY ELEMENT METHOD FOR REAL CRUSTAL WAVEGUIDES

During this project, we also studied Lg wave attenuation due to rough surfaces in two representative geological profiles in Western China using the boundary element (BE) method. The topographic and Moho depth data for these waveguides are from Fan and Lay (1998). The first path is from the epicenter of June 29, 1995 event (focal depth 15 km, latitude 51.923N and longitude 103.075E) to station WMQ. The second path is from the epicenter of June 2, 1990 event (focal depth 17 km, latitude 32.45N and longitude 92.81E) to station WMQ. These waveguide models are shown in Figures 9 and 10, respectively. The source time function used for calculating synthetic seismograms is a Ricker wavelet with a dominant frequency of 1.0 Hz. For the second event, Lg blockage has been observed, while for the first event, no Lg blockage is observed. From Figure 9, we see that the Moho discontinuity of the first waveguide is relatively flat. The crustal thickness is larger (over 40 km) and rather uniform throughout the entire waveguide. The surface roughness is locally dramatic (over 2 km) but generally moderate. The energy decay curve in Figure 9 shows strong fluctuations correlated with the topography. The overall shape of the energy decay curve is relatively stable, especially beyond 1000 km where the energy has been trapped in the waveguide and the attenuation is weak. The model with Lg blockage shows a completely different waveguide structure. The large lateral variations of

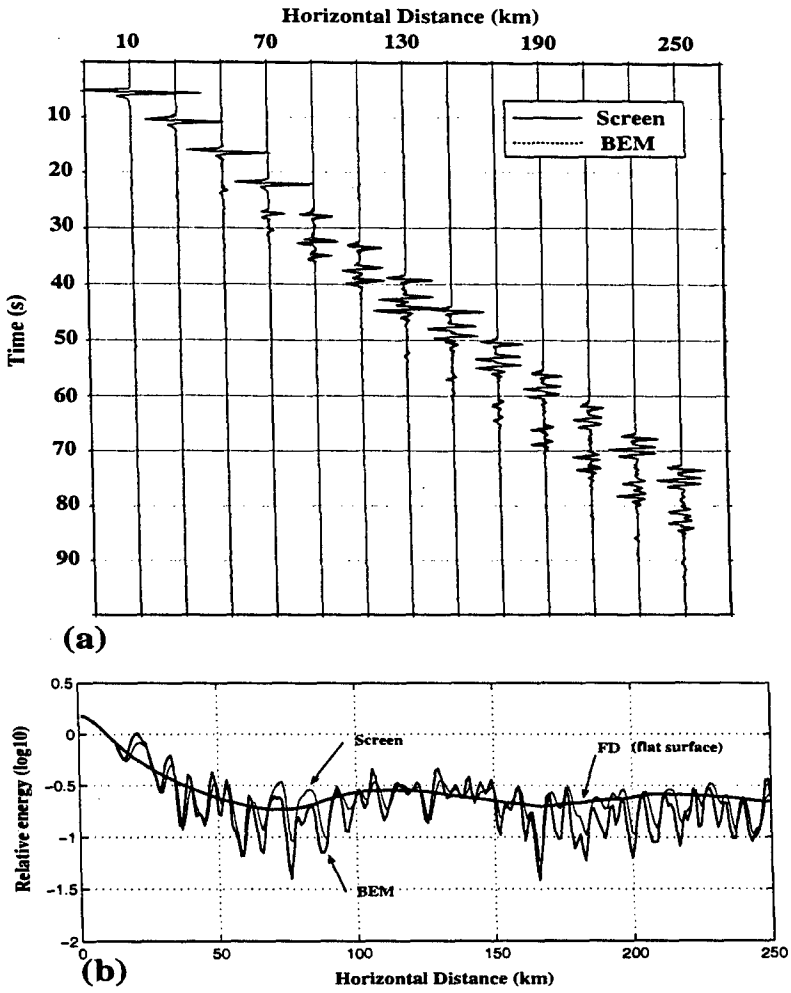

Figure 5. Comparison between the non-conformal screen method and BE method for a crustal waveguide with a rough random surface. (a) Synthetic seismograms, (b) Energy distribution with horizontal distance.

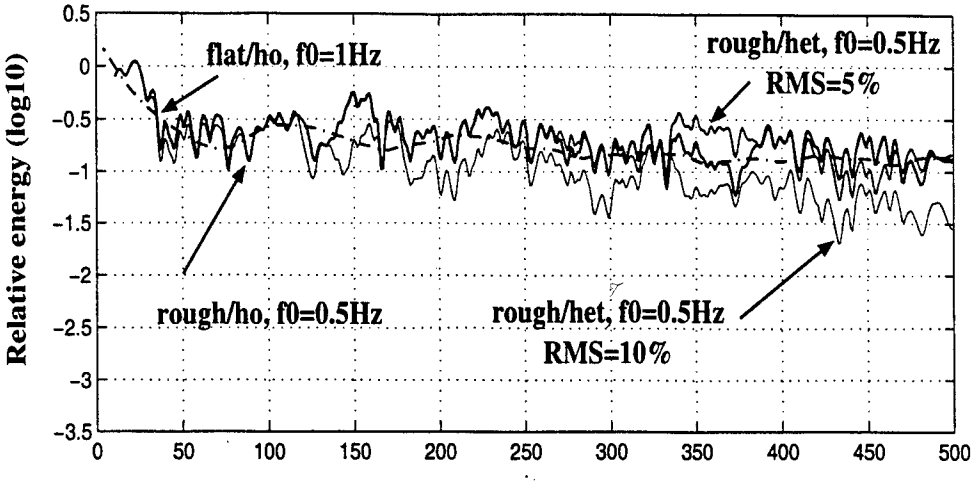

Figure 6. Lg wave attenuation versus horizontal distances. A random medium whose correlation lengths are $6km$ in range and $4km$ in depth, and RMS velocity fluctuations are 5% and 10%, respectively. Source is located at a depth of $8km$, the dominant frequency (f0) of source time function is 0.5Hz. "rough" in the Figure means the crust with rough topography, and "ho" and "het" mean the crusts which are homogeneous and inhomogeneous, respectively.

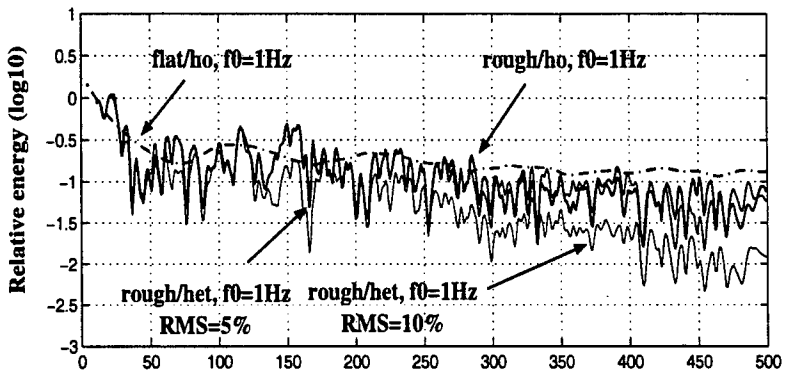

Figure 7. Lg wave attenuation versus horizontal distances. A random medium whose correlation lengths are $6km$ in range and $4km$ in depth, and RMS velocity fluctuations are 5% and 10%, respectively. Source is located at a depth of $8km$, the dominant frequency (f0) of source time function is 1Hz. "rough" in the Figure means the crust with rough topography, and "ho" and "het" mean the crusts which are homogeneous and inhomogeneous, respectively.

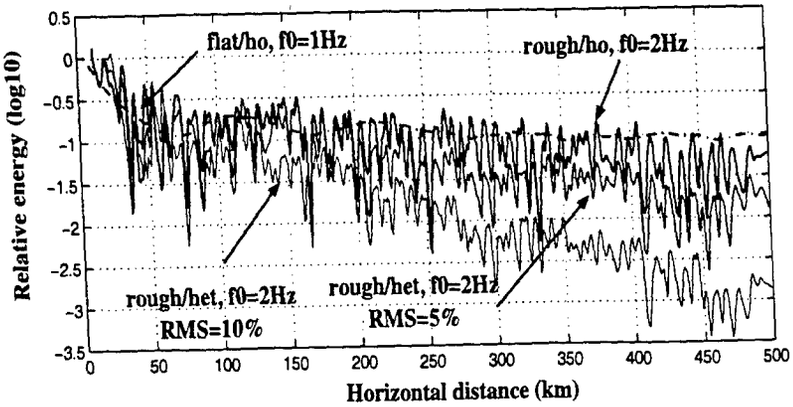

Figure 8. Lg wave attenuation versus horizontal distances. A random medium whose correlation lengths are $6km$ in range and $4km$ in depth, and RMS velocity fluctuations are 5% and 10%, respectively. Source is located at a depth of $8km$, the dominant frequency (f0) of source time function is 2Hz. "rough" in the Figure means the crust with rough topography, and "ho" and "het" mean the crusts which are homogeneous and inhomogeneous, respectively.

topography and the shallowing Moho discontinuity rapidly change the crust into a necking structure after 800 km (Figure 10). The anomalous crustal necking may be responsible for the Lg blockage. Although current calculations are limited to lower frequencies (less than 2 Hz), the energy decay curve shows a rapid attenuation near the necking structure.

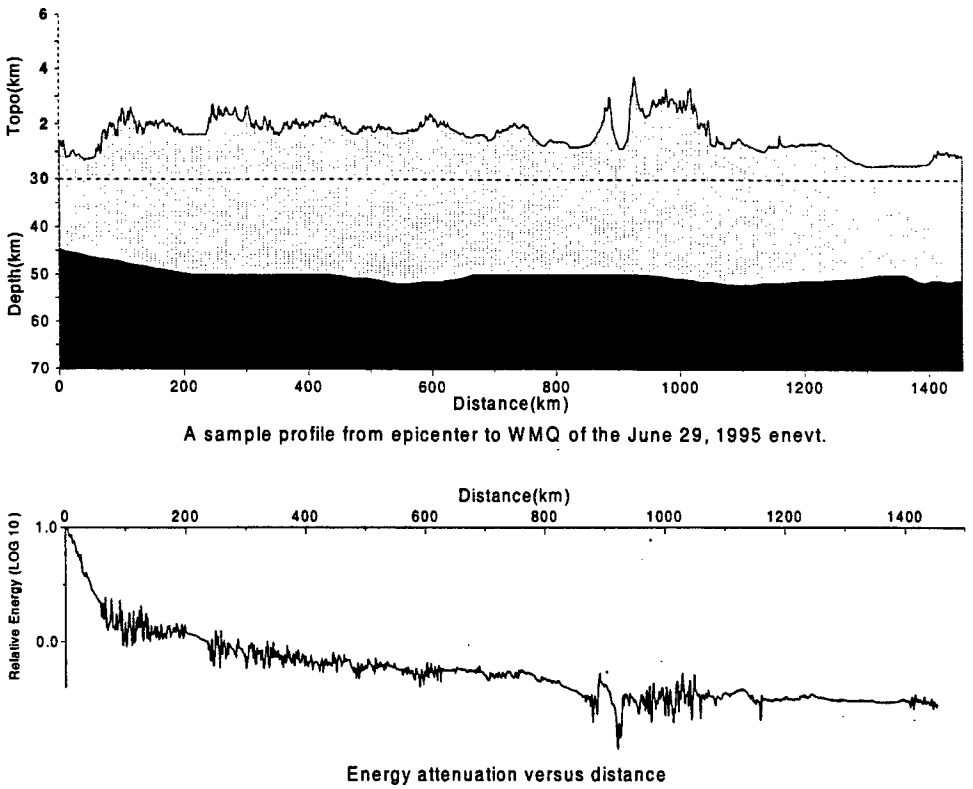

Figure 9. Energy attenuation versus distance for the path without Lg wave blockage in the Tibet region. The model is from the event of June 29, 1995, with the location of 51.923N and 103.075E, the magnitude of 5.6 and the source depth of 15 km.

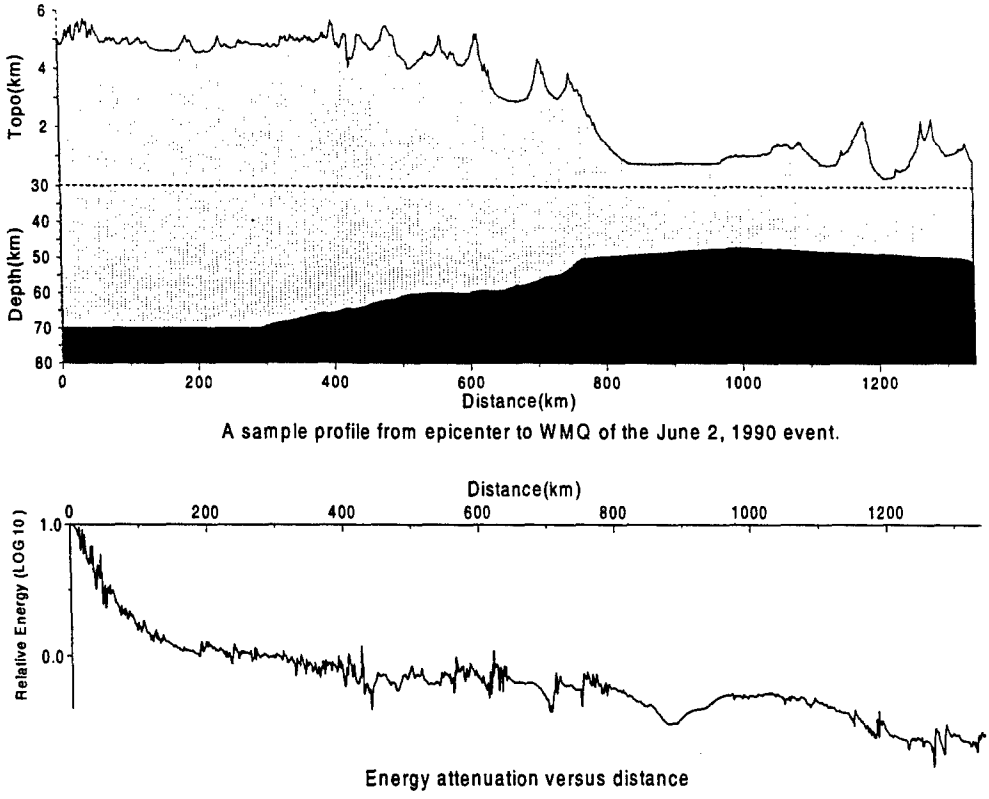

Figure 10. Energy attenuation versus distance for the path without Lg wave blockage in the Tibet region. The model is from the event of June 2, 1990, with the location of 32.45N and 92.81E, the magnitude of 5.5 and the source depth of 17 km.

3. P-SV CASE

Another new development in this project is that the 2D P-SV elastic complex screen method has been applied to Lg wave simulation in crustal waveguides with a flat surface by incorporating plane wave reflection coefficients in the elastic complex screen method. Body waves including the reflected and converted waves can be calculated by real wavenumber integration, surface waves (Rayleigh waves) can be done with imaginary wavenumber integration. Numerical tests show excellent agreement with the theory.

For P-SV elastic wave one-way propagation in heterogeneous crustal waveguides, the derivation and application of screen propagators is much more complicated. Unlike the case of SH waves, the image method of generating the half-space Green's function cannot be used to account for the effect of free surface.

Figure 11 illustrates the principle of the method. Since the screen method is a forward marching algorithm, the re-application of reflection coefficients for each forward step will contribute extra energy, already taken in the last step, to reflections. To avoid extra energy contributions to reflections, we extend the model twice in the vertical direction from the free surface; the extended part has the parameters of the background medium and will be used to keep records of the upgoing waves which can be used for the calculation of reflected/converted waves by the free surface. The complex screen method will be applied to such an extended model for elastic wave simulation. For each forward step we apply the reflection coefficient formulas to the incident field (only to upgoing waves) to calculate the reflections and conversions from the free surface. Figure 1 also shows such a process by an upgoing ray from source. Knowing the reflections and conversions , we calculate the scattered field of the reflected fields using the complex screen method and then combine the scattered field into the incident field to obtain the new incident field. In this section, a simple description of the complex screen method and reflection coefficient formulas is given.

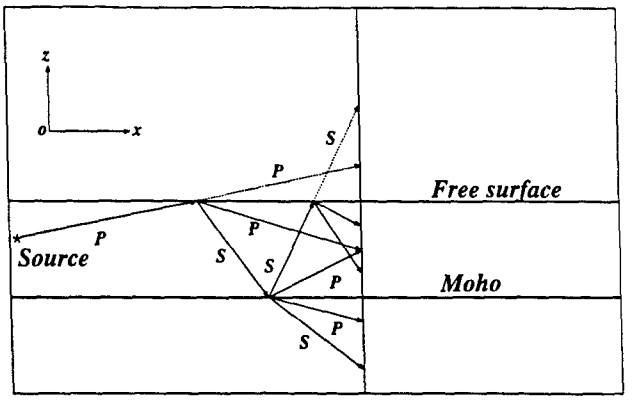

Figure 11. Illustration of the screen method.

3.1 COMPLEX SCREEN PROPAGATOR FOR ELASTIC WAVES

A complete derivation of the complex screen method for modeling elastic waves can be found in Wu (1994). A short review of the method for forward scattering is given in this section. Suppose that the parameters of the elastic medium and the total wave field can be expressed as

$$\begin{aligned} \rho(\mathbf{x}) &= \rho_0 + \delta\rho(\mathbf{x}) \\ \alpha(\mathbf{x}) &= \alpha_0 + \delta\alpha(\mathbf{x}) \\ \beta(\mathbf{x}) &= \beta_0 + \delta\beta(\mathbf{x}) \end{aligned}$$

and

$$\mathbf{u}(\mathbf{x}) = \mathbf{u}_0(\mathbf{x}) + \mathbf{U}(\mathbf{x})$$

where ρ_0, α_0 and β_0 are the parameters of the background medium, $\delta\rho(\mathbf{x})$, $\delta\alpha(\mathbf{x})$ and $\delta\beta(\mathbf{x})$ are the corresponding perturbations, $\mathbf{u}_0(\mathbf{x})$ and $\mathbf{U}(\mathbf{x})$ are the incident field and the scattered field, $\mathbf{X} = x\mathbf{e}_x + z\mathbf{e}_z$ is a 2-D position vector in Cartesian coordinates. We take $\mathbf{e}_x$ to be the primary propagation direction perpendicular to the thin slab. The incident field $\mathbf{u}_0(\mathbf{x})$ at x', e.g., the entrance of the thin slab, can be decomposed into a superposition of plane P and S waves

$$\mathbf{u}_0(\mathbf{x}) = \frac{1}{4\pi^2}\int dk \left[\mathbf{u}_0^P(k,x') + \mathbf{u}_0^S(k,x')\right] e^{ikz} \tag{42}$$

where k is the transverse wavenumber of plane waves. Superscripts P and S denote P and S waves, respectively. The forward propagated field is composed of the primary wave and forward scattered P and S waves. Therefore, at x_1 the exit of the slab, it can be expressed as

$$\mathbf{u}_f(z,x_1) = \frac{1}{4\pi^2}\int dk \left[\mathbf{u}_f^P(k,x_1) + \mathbf{u}_f^S(k,x_1)\right] e^{ikz} \tag{43}$$

where

$$\mathbf{u}_f^P(k,x_1) = \left\{e^{i\gamma_\alpha \Delta x}\mathbf{u}_0^P(k,x') + \mathbf{u}_f^{PP}(k,x_1) + \mathbf{u}_f^{SP}(k,x_1)\right\} \tag{44}$$

$$\mathbf{u}_f^S(k,x_1) = \left\{e^{i\gamma_\beta \Delta x}\mathbf{u}_0^S(k,x') + \mathbf{u}_f^{SS}(k,x_1) + \mathbf{u}_f^{PS}(k,x_1)\right\} \tag{45}$$

where γ_α and γ_β are x components of P and S wavenumbers in the background medium. $\Delta x = x_1 - x'$ is the thickness of the thin slab. Subscript f denotes forward scattering, and PP, PS, SP and SS indicate the scattering between different wave types. Under the complex screen approximation, equations (44) and (45) can be expressed by

$$\begin{aligned} u_f^P(k,x_1) &= e^{i\gamma_\alpha \Delta x}u_0^P(k,x') + u_f^{SP}(k,x_1) \\ &= \hat{k}_\alpha e^{i\gamma_\alpha \Delta x}\int dz e^{ikz}u_0^P(x',z)e^{-ik_\alpha \tilde{\alpha}(x',z)\Delta x} + u_f^{SP}(k,x_1) \end{aligned} \tag{46}$$

$$\begin{aligned} u_f^S(k,x_1) &= e^{i\gamma_\beta \Delta x}u_0^S(k,x') + u_f^{PS}(k,x_1) \\ &= e^{i\gamma_\beta \Delta x}\hat{k}_\beta \times \left\{\hat{k}_\beta \times \int dz e^{-ikz} \times \mathbf{u}_0^S(z,x')e^{-ik_\beta \tilde{\beta}(x',z)\Delta x}\right\} \\ &\quad + u_f^{PS}(k,x_1) \end{aligned} \tag{47}$$

where

$$\begin{aligned} u_f^{PS}(k,x_1) &= ik_\beta e^{i\gamma_\beta \Delta x}\Delta x \eta(\Delta x)\hat{k}_\beta \times \left\{\hat{k}_\beta \times \int dz e^{ikz} \times \mathbf{u}_0^P(z,x')\right. \\ &\quad \left.\left[\left(\frac{\beta_0}{\alpha_0} - \frac{1}{2}\right)\frac{\delta\rho(z,x')}{\rho_0} + 2\frac{\beta_0}{\alpha_0}\frac{\delta\beta(z,x')}{\beta_0}\right]\right\} \end{aligned} \tag{48}$$

$$\begin{aligned} u_f^{SP}(k,x_1) &= -ik_\alpha e^{i\gamma_\alpha \Delta x}\Delta x \eta(\Delta x)^* \left\{\hat{k}_\beta \cdot \int dz e^{-ik\cdot z}\mathbf{u}_0^S(z,x')\right. \\ &\quad \left.\left[\left(\frac{\beta_0}{\alpha_0} - \frac{1}{2}\right)\frac{\delta\rho(z,x')}{\rho_0} + 2\frac{\beta_0}{\alpha_0}\frac{\delta\beta(z,x')}{\beta_0}\right]\right\} \end{aligned} \tag{49}$$

where

$$\eta(\Delta x) = sinc\left[\frac{(k_\beta - k_\alpha)}{2}\Delta x\right]e^{-\frac{i}{2}(k_\beta - k_\alpha)\Delta x} \tag{50}$$

and

$$\gamma_\alpha = (k_\alpha^2 - k^2)^{1/2}, \quad \gamma_\beta = (k_\beta^2 - k^2)^{1/2}\ . \tag{51}$$

$k_\alpha = \omega/\alpha_0$ and $k_\beta = \omega/\beta_0$ are P and S wavenumbers, α_0 and β_0 are P and S velocities of the background medium. The unit wavenumber vectors $\hat{k}_\alpha$ and $\hat{k}_\beta$ are given by

$$\hat{k}_\alpha = \mathbf{k}_\alpha/k_\alpha, \quad \hat{k}_\beta = \mathbf{k}_\beta/k_\beta \tag{52}$$

Equations (46-49) are the dual-domain formulation of the complex screen method. The incident fields u_0^P and u_0^S interact with screens (i.e., heterogeneities) in the space domain, but propagate in the wavenumber domain. We combine the common type scatterings (P-P and S-S) with incident fields (u_0^P and u_0^S) into pure phase screens to ensure stability of the method for models with large contrasts.

3.2 FREE-SURFACE REFLECTIONS OF PROPAGATING P-SV WAVES

From the screen method, the incident P and S waves at $x = x'$ can be expressed as a superposition of plane waves by

$$\mathbf{u}_0^P(x', z) = \int_{-\infty}^{\infty} dk \mathbf{u}_0^P(k, x') e^{ikz} \tag{53}$$

$$\mathbf{u}_0^S(x', z) = \int_{-\infty}^{\infty} dk \mathbf{u}_0^S(k, x') e^{ikz}. \tag{54}$$

Applying the reflection coefficients, the reflected P and S waves due to an incident P wave can be expressed by

$$\mathbf{u}^{PP}(x, z) = e^{i\gamma_\alpha(x-x')} \int dK_z |\mathbf{u}_0^P(K_z, x')| \acute{P}\grave{P}\hat{\mathbf{a}}_1 e^{-iK_z z} \tag{55}$$

$$\mathbf{u}^{PS}(x, z) = e^{i\gamma_\alpha(x-x')} \int dK_z |\mathbf{u}_0^P(K_z, x')| \acute{P}\grave{S}\hat{\mathbf{a}}_2 e^{-iK_z^* z} \tag{56}$$

where $\gamma_\alpha = \sqrt{k_\alpha^2 - K_z^2}$ is the propagating wavenumber for P waves (here in the x-direction) and $K_z^* = \sqrt{k_\beta^2 - k_\alpha^2 + K_z^2}$ is the transverse wavenumber of the converted S wave determined by Snell's law. Unit vectors are $\hat{\mathbf{a}}_1 = (\gamma_\alpha, -K_z)/k_\alpha$ and $\hat{\mathbf{a}}_2 = (K_z^*, \gamma_\alpha)/k_\beta$. $|\mathbf{u}_0^P(K_z, x')|$ is the scalar spectrum of incident P wave with transverse wavenumber K_z (here in the z-direction). The reflected P and S waves due to the incident plane S wave can be obtained by

$$\mathbf{u}^{SP}(x, z) = e^{i\gamma_\beta(x-x')} \int dK_z |\mathbf{u}_0^S(K_z, x')| \acute{S}\grave{P}\hat{\mathbf{a}}_3 e^{-iK_z'^* z} \tag{57}$$

$$\mathbf{u}^{SS}(x, z) = e^{i\gamma_\beta(x-x')} \int dK_z |\mathbf{u}_0^S(K_z, x')| \acute{S}\grave{S}\hat{\mathbf{a}}_4 e^{-iK_z z} \tag{58}$$

where $\gamma_\beta = \sqrt{k_\beta^2 - K_z^2}$ is the propagating wavenumber for S waves (here in the x-direction) and $K_z'^* = \sqrt{k_\alpha^2 - k_\beta^2 + K_z^2}$ is the transverse wavenumber of the reflected P wave. Unit vectors are $\hat{\mathbf{a}}_3 = (\gamma_\beta, -K_z'^*)/k_\alpha$ and $\hat{\mathbf{a}}_4 = (K_z, \gamma_\beta)/k_\beta$. $|\mathbf{u}_0^S(K_z, x')|$ is the scalar spectrum of incident S wave with transverse wavenumber K_z. $\acute{P}\grave{P}$, $\acute{P}\grave{S}$, $\acute{S}\grave{P}$ and $\acute{S}\grave{S}$ in equations (55–58) are reflection

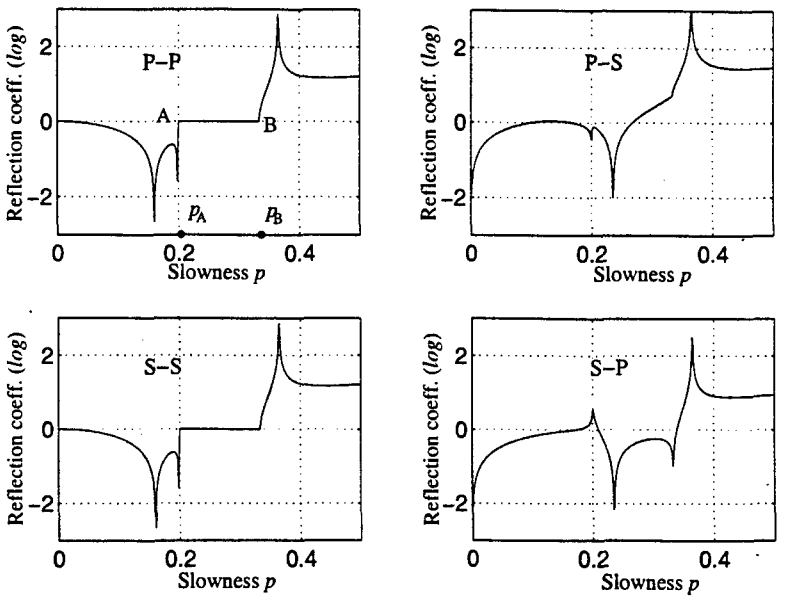

Figure 12. Reflection coefficients(in log) on free surface versus horizontal slowness. Elastic half-space has $\alpha = 5km/s$ and $\beta = 3km/s$. p_A corresponds to P slowness and p_S to S slowness.

coefficients for the free surface (Aki and Richards, 1980). Figure 12 is an example of those reflection coefficients versus horizontal slowness (ray parameter p). In Figure 12 p_A corresponds to P slowness (inverse velocity) and p_B to S slowness. For $p < p_A$, P and S waves are both homogeneous waves, their transverse wavenumbers are real. For $p > p_B$, P and S waves are both inhomogeneous waves, their transverse wavenumbers are imaginary. For $p_A < p < p_B$, P wave is inhomogeneous while S wave is homogeneous. A Rayleigh pole is located at the region of $p > p_B$. In general, we can calculate all of the reflected waves using equations (55−58), once the incident fields $|\mathbf{u}_0^P|$ and $|\mathbf{u}_0^S|$ are known. However, numerically, it is more convenient to separate the calculation of equations (55−58) into homogeneous and inhomogeneous waves, respectively.

For homogeneous waves, equations (55) and (58) (common-type) can be implemented by the FFT. However, the reflected waves of converted-type cannot be directly implemented by the FFT because a nonlinear relationship exists between K_z and K_z^* for P-S (or K_z and $K_z'^*$ for S-P). Although we can obtain uniform samples with respect to K_z and K_z^* (or K_z and $K_z'^*$) by complex variable interpolation for application of the FFT, numerical tests have shown that the noise due to the interpolation is so strong that the accumulated errors increase very fast with multiple step propagation. In our study, the direct summations over the incident waves ($p < p_A$ for P incidence or $p < p_B$ for S incidence) are performed for calculating the converted reflections.

3.3 SURFACE WAVE PROPAGATION USING SCREEN PROPAGATOR

For inhomogeneous waves such as the Rayleigh wave, transverse wavenumbers are imaginary so that equations (55−58) cannot be calculated by FFT. However, the imaginary transverse wavenumber makes the propagation of inhomogeneous waves simple. The phase advance is only along the horizontal direction. It is easily incorporated into the screen method in the wavenumber domain, once the spectra of the inhomogeneous waves are known. Another important feature of the propagation of inhomogeneous waves is the exponential decay occuring only in the direction perpendicular to propagation. Then the spectra of inhomogeneous waves can be calculated with the Laplace transform.

3.4 NUMERICAL TESTS AND EXAMPLES

Figure 13 shows synthetic seismograms calculated with equations (55−58) for an elastic half-space using only homogeneous waves. A point explosion source is located at a depth of 16 km and the dominant frequency of source time function is 1Hz. The first 4 receivers are placed along the free surface separated from the source by 100∼124 km, and the last 5 receivers are placed in vertical profile at 132 km with depths ranging from 0 to 32 km. The results calculated with the wavenumber integration (WI) method (dashed) are also shown as references. Since the source is deep compared with the propagation distance, the Rayleigh wave is very weak in the exact solution. Figure 13a shows the vertical component of the displacement and 13b shows the horizontal component. From Figure 13 we see that the calculations of the reflection and conversion by the free surface are in excellent agreement with the theory.

Figure 14 shows snapshots generated by the screen method for the Flora-Asnes crustal model in the NORSAR region. The parameters for this model are listed in Table 1. The model has a low velocity layer in the top 1 km and a velocity discontinuity at depth 15 km. The receivers are on the surface. A double-couple source is located at the depth of 16km and has a dominant frequency of 2Hz (Ricker wavelet). We see that both P and S waves are well excited. Most events (direct P and S, head waves, PmP, PmS, pS, mantle wave etc.) can be clearly identified. Figure 15 is the corresponding seismograms.

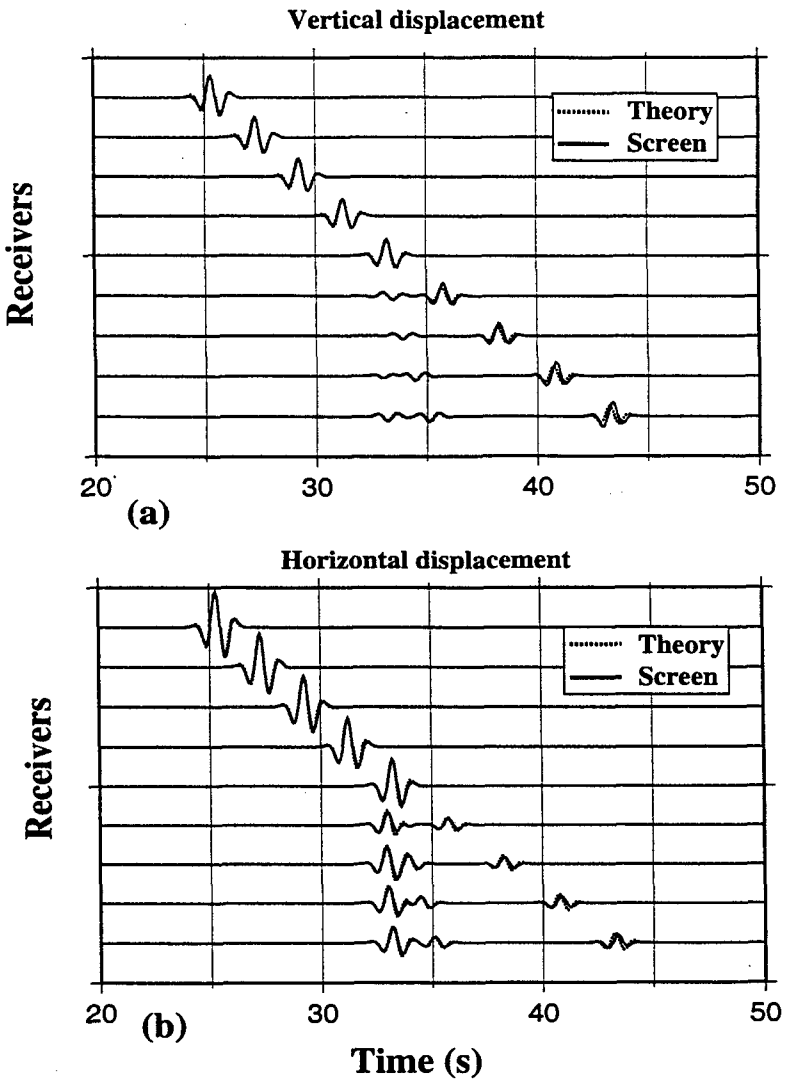

Figure 13. Synthetic seismograms calculated by the elastic screen method (solid) and wavenumber integration method (dashed) for an elastic halfspace. Only homogeneous waves are involved in the results of elastic screen method. (a) shows the vertical components of displacement, (b) shows the horizontal components. A point explosion source is located at the depth of 16km and the dominant frequency of source time function is 1Hz. The first 4 receivers are placed along the free surface separated from the source by 100~124km, and the last 5 receivers are placed in vertical profile at 132km with depths ranging 0~32km.

Table 1. Flora-Asnes crust model

Thickness (km)	α(km/s)	β(km/s)	ρ(g/cm^3)
1.00	5.20	3.00	2.60
14.00	6.00	3.46	2.80
22.00	6.51	3.76	3.00
Infinity	8.05	4.65	3.30

Figure 16 shows a similar result to Figure 14 for the Flora-Asnes crustal model, but an explosive source is used to instead of the double-couple source and the source is located at a depth of 2 km. Figure 17 is the corresponding seismograms. We see that the seismic responses for these two different sources are fairly different, especially for the Lg parts.

Figures 18 shows an example of such a treatment for Rayleigh wave propagating in a homogeneous elastic half-space. The source is located at a depth of 2 km and has a dominant frequency of 0.5 Hz. The vertical receiver array is at a horizontal distance of 100 km. (a) shows the vertical component and (b) shows the horizontal component of Rayleigh waves. The dotted lines are the exact solution. The agreement between the screen calculation and the theory in excellent.

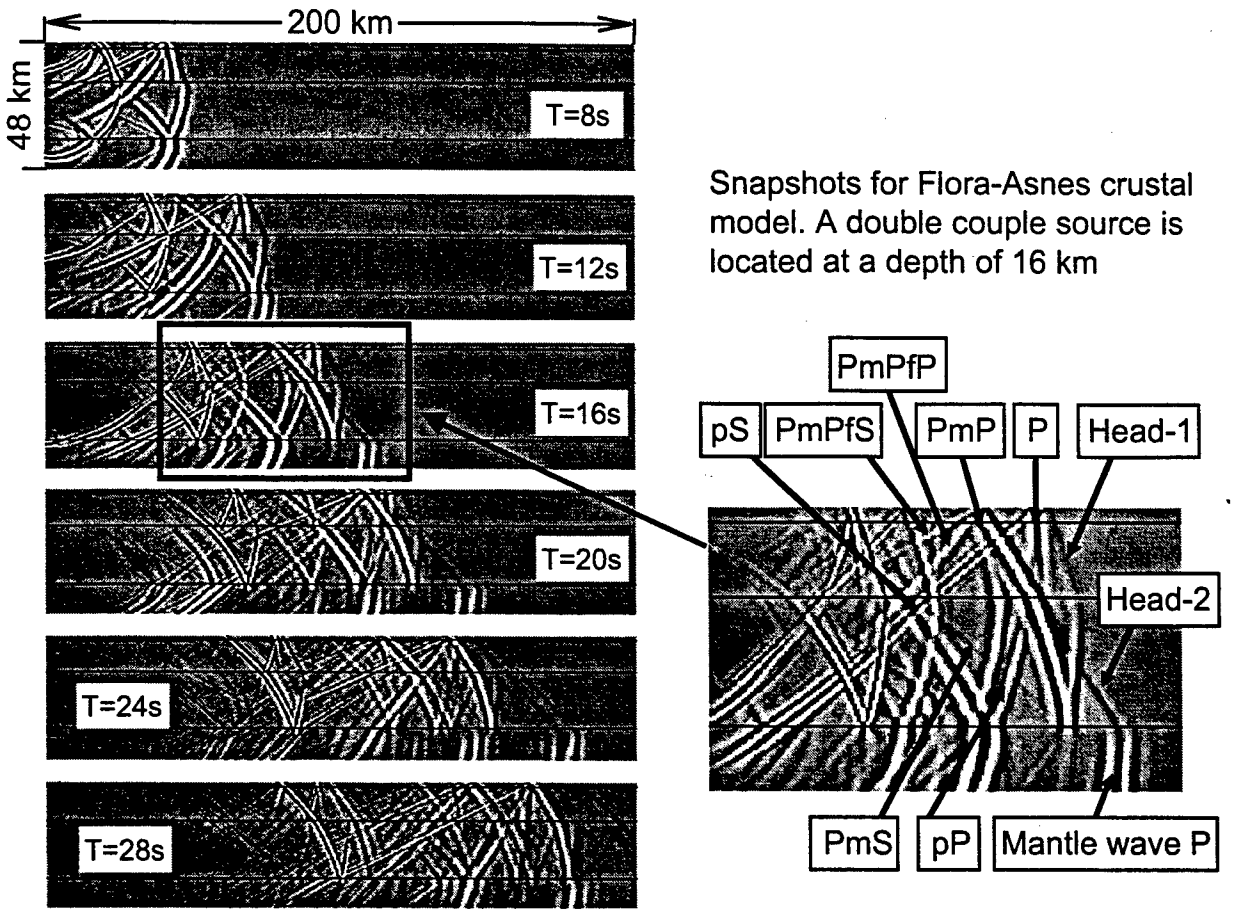

Figure 14. Snapshots (horizontal component of displacement) for Flora-Asnes crustal model using P-SV elastic screen method. A double-couple source is located at a depth of 16 km and has a dominant frequency of 2 Hz. The thicknesses of layers (from top to bottom) are 1 km, 14 km, 22 km and infinity, respectively.

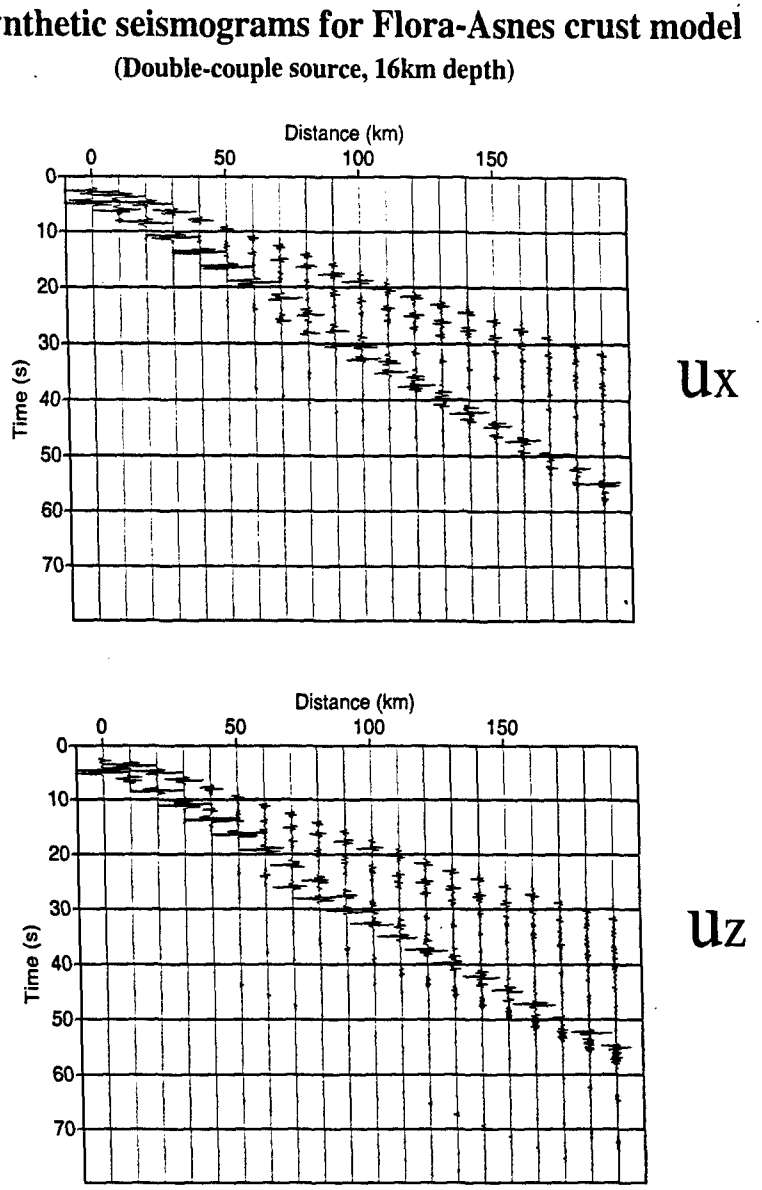

Figure 15. Synthetic seismograms for Flora-Asnes crust model (Table 1). A double-couple source is located at a depth of $16km$ and the source time function has a dominant frequency of $2Hz$

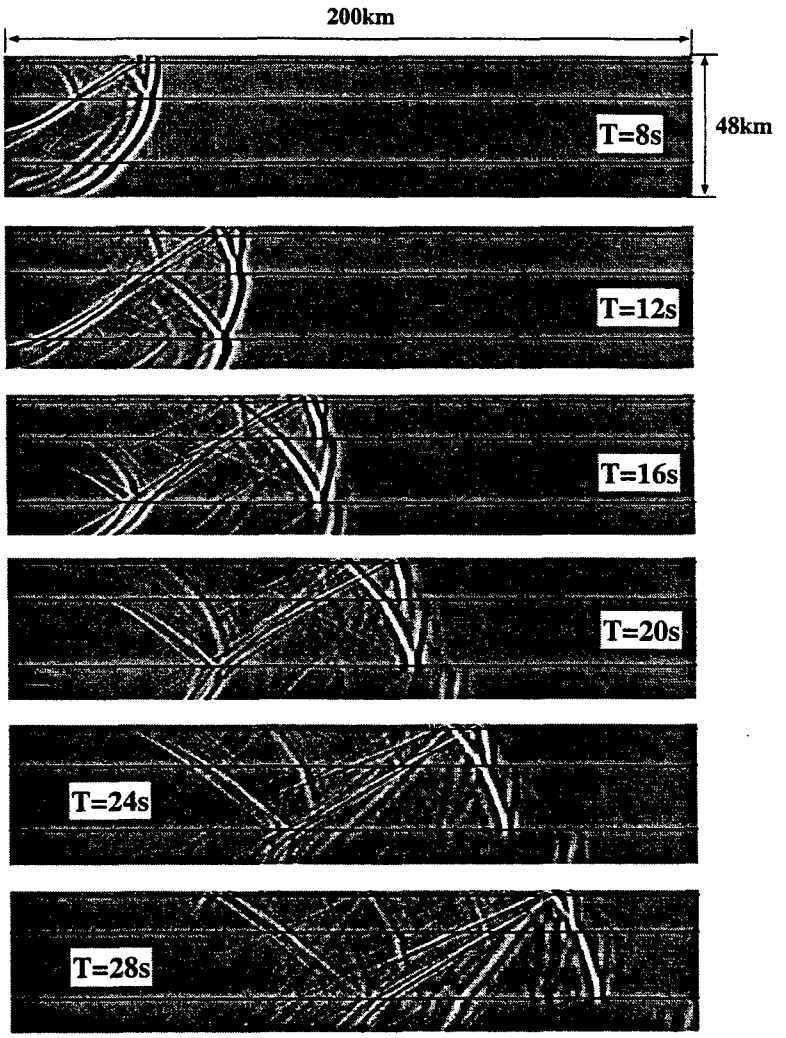

Figure 16. Snapshots for Flora-Asnes crust model (Table 1). An explosive source is located at a depth of $2km$ and the source time function has a dominant frequency of $2Hz$

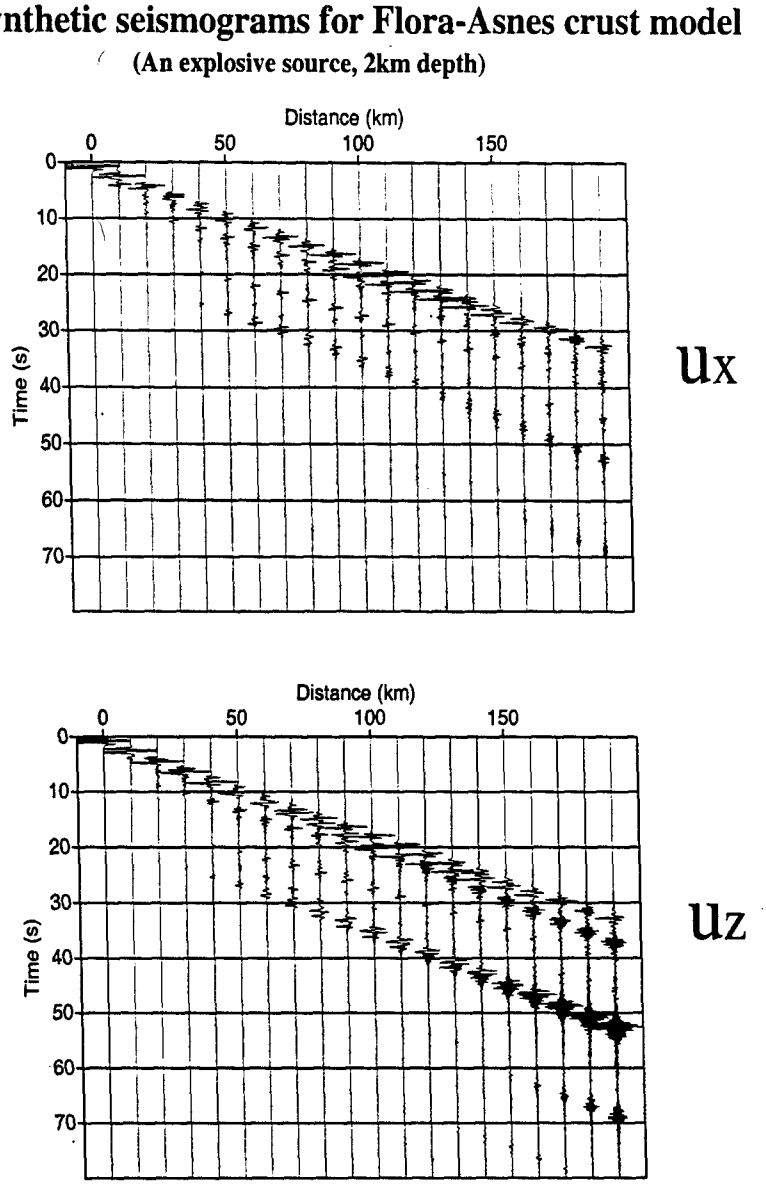

Figure 17. Synthetic seismograms for Flora-Asnes crust model (Table 1). An explosive source is located at a depth of $2km$ and the source time function has a dominant frequency of $2Hz$

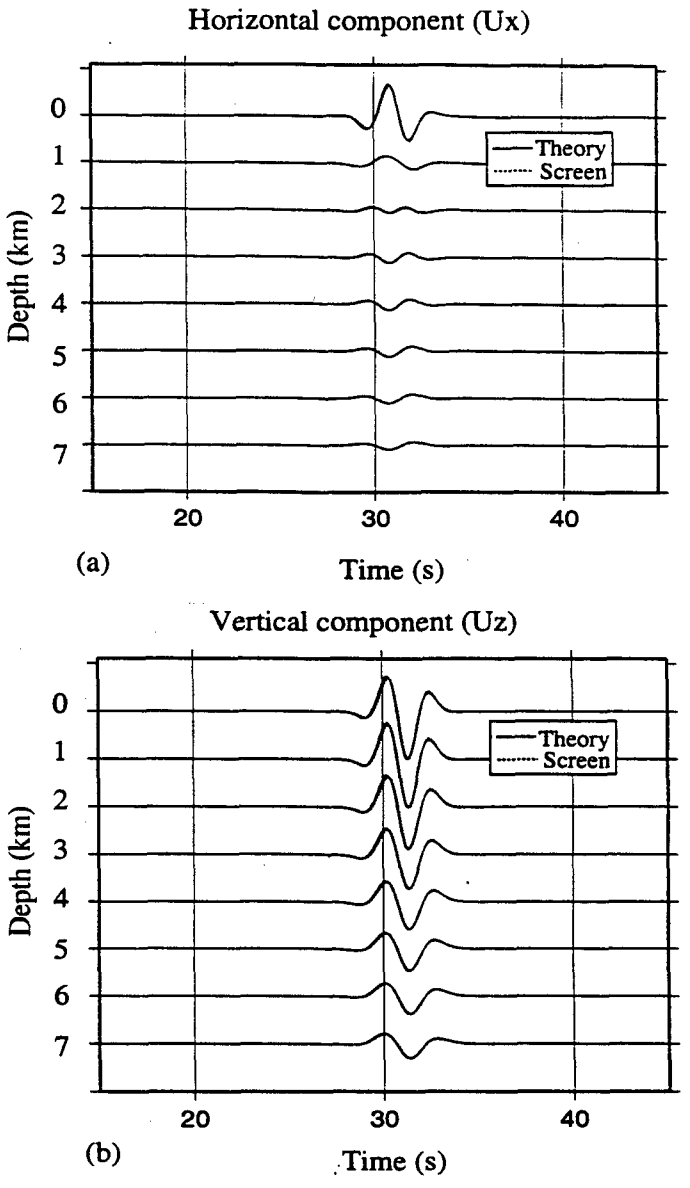

Figure 18. Comparison of synthesized Rayleigh wave (dotted) using screen method with the exact solution (solid). Source is located at the depth of 2km and has a dominant frequency of 0.5Hz. (a) shows the horizontal components of displacement of Rayleigh wave and (b) shows the vertical components. The half-space parameters are $\alpha = 6km/s$ and $\beta = 3.5km/s$.

4. CONCLUSION

Based on the half-space screen propagator developed in our previous project, we successfully extended the method to the case of irregular surface topography by conformal or non-conformal topographic transforms. The validity and potential of the extended method has been numerically demonstrated by comparing the results with the boundary element method. The method can handle the combined effects of small-scale heterogeneities (random media) and rough random topography on Lg wave propagation. For medium size problems, the screen-propagator method is 2-3 orders of magnitude faster than the finite difference method.

In the case of P-SV elastic screen propagators, plane wave reflection calculations have been incorporated into the elastic screen method for Lg wave simulation. Due to the presence of the surface wave (Rayleigh wave), all wavenumber components (real or imaginary parts) must be included. Body waves including the reflected and converted waves can be calculated by real wavenumber integration, surface waves (Rayleigh waves) can be done with imaginary wavenumber integration. Numerical tests against the wavenumber integration method show excellent agreement. An example of simulated Lg wave propagation in Flora-Asnes crust model has demonstrated the promise of simulating path effects in different regions for various discriminants in the monitoring system, such as P_n/L_g, S_n/L_g, etc.

5. REFERENCES

Aki, K., and Richards, P.G. (1980), *Quantitative Seismology: Theory and Methods, Vol. 1 and 2*, W.H. Freeman, New York. (UNCLASSIFIED)

Beillis, A. and Tappert, F.D. (1979), *Coupled mode analysis of multiple rough surface scattering*, J. Acoust. Soc. Am., *66*, 811-826. (UNCLASSIFIED)

Fan G. and Lay, T. (1998), *Statistical analysis of irregular wave-guide influence on regional seismic discriminants in China*, Bull. Seis. Soc. Am., *88*, 74-88. (UNCLASSIFIED)

Fan G. and Lay, T. (1998), *Statistical analysis of irregular wave-guide influence on regional seismic discriminants in China: Additional results for P_n/S_n, P_n/L_g, and P_g/S_n*, Bull. Seis. Soc. Am., *88*, 1504-1510. (UNCLASSIFIED)

Herrmann, R.B., Mokhtar, T.A., Raoof, M., and Ammon, C. (1997), *Wave propagation-16Hz to 60 sec*, Proceedings of the 19th Annual Seismic Research Symposium on Monitoring a Comprehensive Nuclear-Test-Ban Treaty, 495-503, September 23-25. (UNCLASSIFIED)

Huang, L.J., Fehler, M.C., Wu, R.S. (1999), *Extended local Born Fourier migration method*, Geophysics, *64*, 1524-1534. (UNCLASSIFIED)

Huang, L.J., Fehler, M.C., Roberts, P.M., and Burch, C.C. (1999), *Extended local Rytov Fourier migration method*, Geophysics, *64*,1535-1545. (UNCLASSIFIED)

Huang, L.J. and Wu, R.S. (1996), *3D prestack depth migration with acoustic pseudo-screen propagators*, Mathematical methods in geophysical imaging IV, SPIE, *2822*, 40-51. (UNCLASSIFIED)

Jin, S. and Wu, R.S. (1999), *Depth migration with a windowed screen propagator*, Journal of Seismic Exploration, *8*, 27-38. (UNCLASSIFIED)

Jin, S., Wu, R.S., and Peng, C. (1999), *Seismic depth migration with screen propagators*, Computational Geoscience, *3*, 321-335. (UNCLASSIFIED)

Lay, T., Fan, G., Wu, R.S., and Xie, X.B. (1999), *Path corrections for regional phase discriminants*, Proceedings of the 21st Annual Seismic Research Symposium on Monitoring

a Comprehensive Nuclear-Test-Ban Treaty, 510-519, September 21-24. (UNCLASSIFIED)

Lay, T. (1996), *Calibration of regional wave discriminants in Diverse Geological environments: Topographic correlations*, Proceedings of the 18th Annual Seismic Research Symposium on Monitoring a Comprehensive Nuclear-Test-Ban Treaty, 209-218, September 4-6. (UNCLASSIFIED)

Liu, Y.B. and Wu, R.S. (1994), *A comparison between phase-screen, finite difference and eigenfunction expansion calculations for scalar waves in inhomogeneous media*, Bull. Seis. Soc. Am., *84*, 1154-1168. (UNCLASSIFIED)

Ni, J., Reese, C., Wu, J., and Zhao, L.S. (1996), *Crustal structure and attenuation in Southern Tibet*, Proceedings of the 18th Annual Seismic Research Symposium on Monitoring a Comprehensive Nuclear-Test-Ban Treaty, 390-399, September 4-6. (UNCLASSIFIED)

Wild, A.J. and Hudson, J.A. (1997), *A geometrical approach to the elastic complex screen*, J. Geophys. Res., *103*, 707-725. (UNCLASSIFIED)

Wu, R.S. (1994), *Wide-angle elastic wave one-way propagation in heterogeneous media and an elastic wave complex-screen method*, J. Geophys. Res., *99*, 751-766. (UNCLASSIFIED)

Wu, R.S. (1996), *Synthetic seismograms in heterogeneous media by one-return approximation*, Pure and Applied Geophysics, *148*, 155-173. (UNCLASSIFIED)

Wu, R.S., and Huang, L.J. (1995), *Reflected wave modeling in heterogeneous acoustic media using the de Wolf approximation*, Mathematical Methods in Geophysical Imaging III, SPIE Proceedings Series, *2571*, 176-186. (UNCLASSIFIED)

Wu, R.S., Huang, L.J., and Xie, X.B. (1995), *Backscattered wave calculation using the De Wolf approximation and a phase-screen propagator*, Expanded Abstracts, SEG *65*th Annual Meeting, 1293-1296. (UNCLASSIFIED)

Wu, R.S., Jin, S., and Xie, X.B. (1996), *Synthetic seismograms in heterogeneous crustal waveguides using screen propagators*, Proceedings of the 18th Annual Seismic Research Symposium on Monitoring a Comprehensive Nuclear-Test-Ban Treaty, 291-300, September 4-6. (UNCLASSIFIED)

Wu, R.S., Jin, S., and Xie, X.B. (2000a), *Seismic wave propagation and scattering in heterogeneous crustal waveguides using screen propagators*: I SH waves, Bull. Seism. Soc. Am., *90*, 401-413. (UNCLASSIFIED)

Wu, R.S., Jin, S., and Xie, X.B. (2000b), *Energy partition and attenuation of Lg waves by numerical simulations using screen propagators*, Phys. Earth and Planet. Inter., *120*, 227-243. (UNCLASSIFIED)

Wu, R.S., Jin, S., Xie, X.B., and Lay, T. (1997), *Verification and applications of GSP (Generalized screen propagators) method for regional wave propagation*, Proceeding of 19th Annual Seismic Research Symposium on Monitoring a Comprehensive Nuclear-Test-Ban Treaty, 552-561. (UNCLASSIFIED)

Wu, R.S. and Xie, X.B. (1994), *Multi-screen backpropagator for fast 3D elastic prestack migration*, Mathematical Methods in Geophysical Imaging II, SPIE Proceedings Series, *2301*, 181-193. (UNCLASSIFIED)

Wu, R.S., Xie, X.B., Jin, S., Fu, L., and Lay, T. (1998), *Seismic wave propagation and scattering in heterogeneous crustal waveguides using screen propagators*, Proceedings of the 20th Annual Seismic Research Symposium on Monitoring a Comprehensive Nuclear-Test-Ban Treaty, 201-210, September 21-23. (UNCLASSIFIED)

Wu, R.S., Xie, X.B., and Wu, X.Y. (1999), *Lg wave simulations in heterogeneous crusts with irregular topography suing half-space screen propagators*, Proceedings of the 21st Annual Seismic Research Symposium on Monitoring a Comprehensive Nuclear-Test-Ban Treaty, 683-693, September 21-24. (UNCLASSIFIED)

Wu, R.S., Xie, X.B., and Wu, X.Y. (2000), *Lg wave propagation using SH and P-SV screen propagators in heterogeneous crusts with irregular topography*, Proceedings of the 22nd Annual Seismic Research Symposium on Monitoring a Comprehensive Nuclear-Test-Ban Treaty. (UNCLASSIFIED)

Wu, R.S., Xu, Z., and Li, X.P. (1994), *Heterogeneity spectrum and scale-anisotropy in the upper crust revealed by the German continental deep-drilling (KTB) holes*, Geophysi. Res. Lett., *21*, 911-914. (UNCLASSIFIED)

Wu, X.Y. and Wu, R.S. (1999), *Wide-angle thin-slab propagator with phase matching for elastic wave modeling*, Expanded Abstracts, SEG *69*th Annual Meeting, 1867-1870. (UNCLASSIFIED)

Wu, X.Y. and Wu, R.S. (1999), *Lg wave simulation in heterogeneous crusts with surface topography using screen propagators*, Accepted by Geophys. J. Int.. (UNCLASSIFIED)

Xie, X.B. and Wu, R.S. (1995), *A complex-screen method for modeling elastic wave reflections*, Expanded Abstracts, SEG *65*th Annual Meeting, 1269-1272. (UNCLASSIFIED)

Xie, X.B. and Wu, R.S. (1996), *3D elastic wave modeling using the complex screen method*, Expanded Abstracts, SEG *66*th Annual Meeting, 1247-1250. (UNCLASSIFIED)

Xie, X.B. and Wu, R.S. (1998), *Improving the wide angle accuracy of the screen method under large contrast*, Expanded Abstracts, SEG *68*th Annual Meeting, 1811-1814. (UNCLASSIFIED)

Xie, X.B. and Wu, R.S. (1999), *Improving the wide angle accuracy of the screen propagator for elastic wave propagation*, Expanded Abstracts, SEG *69*th Annual Meeting, 1863-1866. (UNCLASSIFIED)

Xie, X.B. and Wu, R.S. (2000), *Modeling elastic wave forward propagation and reflection using the complex-screen method*, J. Acoust. Soc. Am., accepted. (UNCLASSIFIED)

DISTRIBUTION LIST
DTRA-TR-03-1

DEPARTMENT OF DEFENSE

DIRECTOR
DEFENSE INTELLIGENCE AGENCY
BUILDING 6000
WASHINGTON, DC 20340-5100
ATTN: DTIB

DEFENSE RESEARCH AND ENGINEERING
3030 DEFENSE PENTAGON
WASHINGTON, D.C. 20301-3030
ATTN: DIRECTOR

DEFENSE TECHNICAL INFORMATION CENTER
8725 JOHN J. KINGMAN ROAD, SUITE 0944
FT. BELVOIR, VA 22060-6218
2 CYS ATTN: DTIC/OCA

DEFENSE THREAT REDUCTION AGENCY
8725 JOHN J. KINGMAN ROAD MS 6201
FT. BELVOIR, VA 22060-6201
ATTN: TDND, CPT. BARBER

OFFICE OF THE SECRETARY OF DEFENSE
CHEMICAL DEMILITARIZATION AND THREAT REDUCTION OFFICE
1515 WILSON BOULEVARD, SUITE 720
ARLINGTON, VA 22209-2402
ATTN: P. WAKEFIELD
ATTN: DR. S. MANGINO

DEPARTMENT OF THE ARMY

US ARMY SMDC
SMDC-TC-YD
P.O. BOX 1500
HUNTSVILLE, AL 35807 3801
ATTN: B. ANDRE

DEPARTMENT OF THE AIR FORCE

AIR FORCE RESEARCH LABORATORY
29 RANDOLPH ROAD
HANSCOM AFB, MA 01731
ATTN: RESEARCH LIBRARY
ATTN: VSBL, R. RAISTRICK

USAF SENIOR CONSULTANT
1809 PAUL SPRING ROAD
ALEXANDRIA, VA 22307
ATTN: R. BLANDFORD

BUREAU OF VERIFICATION & COMPLIANCE
VC/TA, ROOM 2833
2201 C ST., N.W. WASHINGTON, D.C. 20520
ATTN: RONGSONG JIH

AIR FORCE TECHNICAL APPLICATIONS CTR
1030 S. HIGHWAY AIA
PATRICK AFB, FL 32925 3002
ATTN: CA/STINFO
ATTN: TTR, D. CLAUTER
ATTN: CTI, DR. B. KEMERAIT
ATTN: TT, DR. D. RUSSELL
ATTN: TTR, F. SCHULTZ
ATTN: TTR, G. ROTHE
ATTN: TTR, V. HSU
ATTN: DR. B. NGUYEN
ATTN: DR. E. SMART
ATTN: DR. G. WAGNER
ATTN: DR. M. WOODS

DEPARTMENT OF THE NAVY

NAVAL RESEARCH LABORATORY
4555 OVERLOOK AVE, SW, CODE 7643
WASHINGTON, DC 20375 0001
ATTN: DR. D. DROB

DEPARTMENT OF ENERGY

NATIONAL NUCLEAR SECURITY ADMINISTRATION
1000 INDEPENDENCE AVE SW
WASHINGTON, DC 20585 0420
ATTN: L. CASEY
ATTN: G. KIERNAN

UNIVERSITY OF CALIFORNIA
LAWRENCE LIVERMORE NATIONAL LAB
P.O. BOX 808
LIVERMORE, CA 94551 9900
ATTN: MS L205, DR. D. HARRIS

LOS ALAMOS NATIONAL LABORATORY
P.O. BOX 1663
LOS ALAMOS, NM 87545
ATTN: MS C335, DR. S. R. TAYLOR

PACIFIC NORTHWEST NATIONAL LABORATORY
P.O. BOX 999
1 BATTELEE BOULEVARD
RICHLAND, WA 99352
ATTN: MS P8-20, T. HEIMBIGNER
ATTN: MS K8-29, DR. N. WOGMAN

SANDIA NATIONAL LABORATORIES
MAIL SERVICES
P.O. BOX 5800
ALBUQUERQUE, NM 87185 1164
ATTN: WILLIAM GUYTON

DISTRIBUTION LIST
DTRA-TR-03-1

OTHER GOVERNMENT

DEPARTMENT OF STATE
2201 C STREET NW
WASHINGTON, DC 20520
ATTN: R. MORROW, ROOM 5741

US GEOLOGICAL SURVEY
905 NATION CENTER
12201 SUNRISE VALLEY DR
RESTON, VA 20192
ATTN: W. LEITH

US GEOLOGICAL SURVEY
345 MIDDLEFIELD RD MS 977
MENLO PARK, CA 94025
ATTN: S. DETWEILER
ATTN: DR. W. MOONEY

DEPARTMENT OF DEFENSE CONTRACTORS

BATTELLE
MANAGER, ENERGETIC SYSTEMS &
SECURITY TECHNOLOGIES
505 KING AVE
COLUMBUS, OH 43201-2693
ATTN: NEAL OWENS (7-2-081)

BBN CORPORATION
1300 N 17TH STREET, SUITE 400
ARLINGTON, VA 22209
ATTN: DR. D. NORRIS
ATTN: R. GIBSON
ATTN: J. PULLI

CENTER FOR MONITORING RESEARCH
1953 GALLOWS ROAD, SUITE 260
VIENNA, VA 22182 3997
ATTN: DR. K. L. MCLAUGLHLIN
ATTN: DR. R. WOODWARD
ATTN: DR. R. NORTH
ATTN: DR. X. YANG
ATTN: LIBRARIAN

ENSCO, INC.
5400 PORT ROYAL ROAD
P.O. BOX 1346
SPRINGFIELD, VA 22151 2312
ATTN: D. BAUMGARDT
ATTN: Z. DER

WESTON GEOPHYSICAL CORPORATION
27 BEDFORD ST, SUITE 102
LEXINGTON, MA 02420
ATTN: DR. D. REITER
ATTN: J. LEWKOWICZ
ATTN: DR. A. ROSCA
ATTN: DR. I. TIBULEAC
ATTN: M. JOHNSON

ITT INDUSTRIES
ITT SYSTEMS CORPORATION
1680 TEXAS STREET SE
KIRTLAND AFB, NM 87117 5669
2 CYS ATTN: DTRIAC
ATTN: DARE

TITAN CORPORATION (ATS)
1900 CAMPUS COMMONS DR SUITE 600
RESTON, VA 20191-1535
ATTN: DR. C. P. KNOWLES

MISSION RESEARCH CORPORATION
8560 CINDERBED ROAD, SUITE 700
NEWINGTON, VA 22122
ATTN: DR. M. FISK

MULTIMAX, INC
1441 MC CORMICK DRIVE
LANDOVER, MD 20785
ATTN: DR. I. N. GUPTA
ATTN: W. RIVERS

MULTIMAX, INC
1090 N HIGHWAY A1A SUITE D
INDIANLATIC, FL 32903
ATTN: DR. H. GHALIB

SCIENCE APPLICATIONS INTERNATIONAL
CORP
10260 CAMPUS POINT DRIVE
SAN DIEGO, CA 92121 1578
ATTN: DR.M. ENEVA
ATTN: DR. G. E. BAKER
ATTN: DR. J. STEVENS
ATTN: DR. D. ADAMS

SCIENCE APPLICATIONS INT'L CORP
1227 S. PATRICK DR SUITE 110
SATELLITE BEACH, FL 32937
ATTN: DR. M. FELIX
ATTN: DR. H. GIVEN

URS CORPORATION
566 EL DORADO STREET
PASADENA, CA 91109 3245
ATTN: DR. C. SAIKIA
ATTN: DR. G. ICHINOSE

DIRECTORY OF OTHER (LIBRARIES AND UNIVERSITIES)

BOSTON COLLEGE
INSTITUTE FOR SPACE RESEARCH
140 COMMONWEALTH AVENUE
CHESTNUT HILL, MA 02167
ATTN: DR. D. HARKRIDER

BROWN UNIVERSITY
DEPARTMENT OF GEOLOGICAL SCIENCES
75 WATERMAN STREET
PROVIDENCE, RI 02912 1846
ATTN: PROF. D. FORSYTH

CALIFORNIA INSTITUTE OF TECHNOLOGY
DIVISION OF GEOLOGY & PLANETARY SCIENCES
PASADENA, CA 91125
ATTN: PROF. DONALD V. HELMBERGER
ATTN: PROF. THOMAS AHRENS

UNIVERSITY OF CALIFORNIA BERKELEY
281 MCCONE HALL
BERKELY, CA 94720 2599
ATTN: PROF. B. ROMANOWICZ
ATTN: DR. D. DREGER

UNIVERSITY OF CALIFORNIA
DEPT OF STATISTICS
DAVIS, CA 95616
ATTN: R.H. SHUMWAY, DIV STATISTICS

UNIVERSITY OF CALIFORNIA SAN DIEGO
SCRIPPS INSTITUTION OF TECHNOLOGY
9500 GILMAN DRIVE
LA JOLLA, CA 92093 0225
ATTN: DR.L. DEGROOT - HEDLIN
ATTN: DR. M. HEDLIN
ATTN: PROF. F. VERNON
ATTN: PROF. J. BERGER

UNIVERSITY OF CALIFORNIA SANTA CRUZ
INSTITUTE OF TECTONICS
SANTA CRUZ, CA 95064
ATTN: DR. R. S. WU
ATTN: PROF. T. LAY

UNIVERSITY OF COLORADO BOULDER
DEPT OF PHYSICS, CAMPUS BOX 390
BOULDER, CO 80309
ATTN: DR.R. ENGDAHL
ATTN: M. RITZWOLLER
ATTN: PROF. C. ARCHAMBEAU

COLUMBIA UNIVERSITY
LAMONT DOHERTY EARTH OBSERVATORY
PALISADES, NY 10964
ATTN: DR. J. XIE
ATTN: DR. W. Y. KIM
ATTN: PROF. P.G. RICHARDS
ATTN: DR. M. TOLSTOY

UNIVERSITY OF CONNECTICUT
DEPARTMENT OF GEOLOGY & GEOPHYSICS
STOORS, CT 06269 2045
ATTN: PROF. V.F. CORMIER, U-45, ROOM 207

CORNELL UNIVERSITY
DEPARTMENT OF GEOLOGICAL SCIENCES
3126 SNEE HALL
ITHACA, NY 14853
ATTN: PROF. M.A. BARAZANGI

HARVARD UNIVERSITY
HOFFMAN LABORATORY
20 OXFORD STREET
CAMBRIDGE, MA 02138
ATTN: PROF. A. DZIEWONSKI
ATTN: PROF. G. EKSTROM

INDIANA UNIVERSITY
DEPARTMENT OF GEOLOGICAL SCIENCES
1005 10TH STREET
BLOOMINGTON, IN 47405
ATTN: PROF. G. PAVLIS

IRIS
1200 NEW YORK AVENUE, NW SUITE 800
WASHINGTON, DC 20005
ATTN: DR. D. SIMPSON

IRIS
1408 NE 45TH ST #201
SEATTLE, WA 98105
ATTN: DR. T. AHERN

MASSACHUSETTS INSTITUTE OF TECHNOLOGY
EARTH RESOURCES LABORATORY
42 CARLETON STREET
CAMBRIDGE, MA 02142
ATTN: DR. W. RODI
ATTN: PROF. M.N. TOKSOZ

MICHIGAN STATE UNIVERSITY LIBRARY
450 ADMINISTRATION BUILDING
EAST LANSING, MI 48824
ATTN: K. FUJITA

NEW MEXICO STATE UNIVERSITY
DEPARTMENT OF PHYSICS
LAS CRUCES, NM 88003
ATTN: PROF. J. NI
ATTN: PROF. T. HEARN

NORTHWESTERN UNIVERSITY
DEPARTMENT OF GEOLOGICAL SCIENCES
1847 SHERIDAN RD
EVANSTON, IL 60208
ATTN: PROF. E. OKAL

PENNSYLVANIA STATE UNIVERSITY
GEOSCIENCES DEPARTMENT
403 DEIKE BUILDING
UNIVERSITY PARK, PA 16802
ATTN: PROF. C. AMMON
ATTN: PROF. S. ALEXANDER
ATTN: DR. A. NYBLADE

SAN DIEGO STATE UNIVERSITY
DEPARTMENT OF GEOLOGICAL SCIENCES
SAN DIEGO, CA 92182
ATTN: PROF. S. M. DAY

SOUTHERN METHODIST UNIVERSITY
DEPARTMENT OF GEOLOGICAL SCIENCES
P.O. BOX 750395
DALLAS, TX 75275
ATTN: B. STUMP
ATTN: E. HERRIN
ATTN: P. GOLDEN

UNIVERSITY OF HAWAII- MANOA
P.O. BOX 1599
KAILUA-KONA,HI 96745 1599
ATTN: DR. M. A. GARCES

UNIVERSITY OF MISSISSIPPI
1 COLISEUM DRIVE
UNIVERSITY, MS 38677
ATTN: PROF. H. BASS

UNIVERSITY OF SOUTHERN CALIFORNIA
520 SEAVER SCIENCE CENTER
UNIVERSITY PARK
LOS ANGELES, CA 90089 0483
ATTN: PROF. C. G. SAMMIS
ATTN: PROF. T. JORDAN

UNIVERSITY OF WISCONSIN MADISON
1215 W DAYTON ST
MADISON, WI 53706 1600
ATTN: DR. C. THURBER

ST LOUIS UNIVERSITY
EARTH & ATMOSPHERIC SCIENCES
STATION 3507 LACLEDE AVE
ST LOUIS, MO 63103
ATTN: PROF. B. J. MITCHELL
ATTN: PROF. R. HERRMAN

UNIVERSITY OF MEMPHIS
3904 CENTRAL AVE
MEMPHIS, TN 38152
ATTN: DR. J. PUJOL

UNIVERSITY OF MEMPHIS
3876 CENTRAL AVE
MEMPHIS, TN 38152
ATTN: DR. C. LANGSTON

UNIVERSITY OF TEXAS AUSTIN
IGS 130
AUSTIN, TX 78712
ATTN: DR. J. PULLIAM

UNIVERSITY OF TEXAS AUSTIN
IGS 131
AUSTIN, TX 78712
ATTN: DR. M. SEN

UNIVERSITY OF TEXAS EL PASO
DEPT OF GEOLOGICAL SCIENCES
EL PASO, TX 79901
ATTN: PROF. G. KELLER
ATTN: DR. D. DOSER
ATTN: DR. A. VELASCO

FOREIGN

AUSTRALIAN GEOLOGICAL SURVEY
ORGANIZATION
CORNER OF JERRAGOMRRRA &
NINDMARSH DRIVE
CANBERRA, ACT 2609
AUSTRALIA
ATTN: D. JESPSON

GEOPHYSICAL INSTITUTE OF ISRAEL
POB 182
LOD, 7100 ISRAEL
ATTN: DR. Y. GITTERMAN
ATTN: DR. A. SHAPIRA

GEOLOGICAL SURVEY OF CANADA
7 OBSERVATORY CRESCENT
OTTAWA K1A 0Y3 ONT
CANADA
ATTN: C. WOODGOLD

I.R.I.G.M. B.P. 68
38402 ST. MARTIN D'HERES
CEDEX, FRANCE
ATTN: DR. M. BOUCHON

MINISTRY OF DEFENSE
PROCUREMENT EXECUTIVE
BLACKNESS, BRIMPTON
READING FG7-4RS ENGLAND
ATTN: DR. D. BOWERS

NTNF/NORSAR
P.O. BOX 51
N-2007 KJELLER, NORWAY
ATTN: DR. F. RINGDAL
ATTN: T. KVAERNA
ATTN: S. MYKKELTVEIT